

1 Dear editor,

2 All the asked corrections have been done and are hereafter highlighted in the text.

3 *The authors should address the following:*

4

5 *Pages, line numbers, are for the document with tracking.*

6

7 *P. 5*

8

9 *L. 119: forecast - > forecasts.*

10

11 *P. 6*

12

13 *L. 152: frame -> framework. Same elsewhere (e.g., L. 187).*

14

15 *P. 8*

16

17 *L. 183: Perhaps: recalled - > summarized.*

18

19 *P. 12*

20

21 *L. 288: "...Medium-Range..."*

22

23 *P. 13*

24

25 *L. 318: "...according to the RMSE and COR indicators..."*

26

27 *P. 15*

28

29 *L. 366: inverse -> invert.*

30

31 *P. 18*

32

33 *Conclusion section: I suggest you introduce acronyms again.*

34

35 *P. 19*

36

37 *L. 462: Indicate where this was reported.*

38 *Jeju Island, South Korea 26 March - 1 April 2014*

39 *International TOVS Study Conferences*

40 *(ITSC)*

41

42 P. 34  
43  
44 L. 691: Indicate COR is in black.  
45  
46 P. 35  
47  
48 L. 698: legends -> legend.  
49  
50 P. 37  
51  
52 L. 711: abscisa -> abscissa.  
53  
54 P. 40  
55  
56 L. 722: Indicate how the CN are identified.

57 | **Comparison of IASI water vapor retrieval with H<sub>2</sub>O-Raman lidar in the framework of**  
58 **the Mediterranean HyMeX and ChArMEx programs**

59 Patrick Chazette, Fabien Marnas, Julien Totems and Xiaoxia Shang

60

61 Laboratoire des Sciences du Climat et de l'Environnement (LSCE), UMR8212, Laboratoire  
62 mixte CEA-CNRS-UVSQ, CEA Saclay, 91191 Gif-sur-Yvette, France.

63

64 Abstract.

65 The Infrared Atmospheric Sounding Interferometer (IASI) is a spaceborne passive sensor of  
66 new generation mainly dedicated to meteorological applications. Operational Level-2  
67 products are available via the European Organisation for the Exploitation of Meteorological  
68 Satellites (EUMETSAT) since several years. In particular, vertical profiles of water vapor  
69 measurements are retrieved from infrared radiances at the global scale. Nevertheless, the  
70 robustness of such products has to be checked because only few validations have been  
71 reported. For this purpose, the field experiments that were held during the HyMeX and  
72 ChArMEx international programs are a very good opportunity. A H<sub>2</sub>O-Raman lidar was  
73 deployed on the Balearic Island of Menorca and operated continuously during ~6 and ~3  
74 weeks during fall 2012 (Hydrological cycle in the Mediterranean eXperiment -HyMeX-) and  
75 summer 2013 (Chemistry-Aerosol Mediterranean Experiment -ChArMEx-), respectively. It  
76 measured simultaneously the water vapor mixing ratio and aerosol optical properties. This  
77 article does not aim to describe the IASI operational H<sub>2</sub>O inversion algorithm, but to compare  
78 the vertical profiles derived from IASI onboard MetOp-A and the ground-based lidar  
79 measurements to assess the reliability of the IASI operational product for the water vapor  
80 retrieval in both the lower and middle troposphere. The links between water vapor contents  
81 and both the aerosol vertical profiles and the air mass origins are also studied. About 30

82 simultaneous observations, performed during nighttime in cloud free conditions, have been  
83 considered. For altitudes ranging from 2 to 7 km, root mean square errors (correlation) of ~0.5  
84 g/kg (~0.77) and ~1.1 g/kg (~0.72) are derived between the operational IASI product and the  
85 available lidar profiles during HyMeX and ChArME<sub>x</sub>, respectively. The values of both root  
86 mean square error and correlation are meaningful and show that the operational Level-2  
87 product of the IASI-derived vertical water vapor mixing ratio can be considered for  
88 meteorological and climatic applications, at least in the framework of field campaigns.

## 89 1 Introduction

90 Satellite observations are powerful tools for meteorological forecasts. Their assimilation in  
91 models lead to an improvement on weather forecasts (e.g. *Collard and McNally, 2009;*  
92 *Bormann et al., 2010*). Among the main components of the atmospheric state, water vapor is  
93 an essential element, which plays a key role in frontogenesis, convection (e.g. *Held and*  
94 *Soden, 2000*), cloud formation and aerosol hydration (e.g. *Larson and Taylor, 1983; Rood et*  
95 *al., 1987; Randriamiarisoa et al., 2006*). In this way, it influences significantly the Earth  
96 climate and the atmospheric chemistry (e.g. *IPCC, 2014*). It is also an energy reservoir that  
97 exchanges with both the atmosphere and the surface through condensation and evaporation  
98 processes via the latent heat flux. Hence, for reliable weather forecasts, the vertical profile of  
99 the water vapor has to be precisely assessed.

100 During several decades, passive radiometers, such as those implemented onboard of the  
101 Television InfraRed Operational Satellite (TIROS) from the National Oceanographic and  
102 Atmospheric Administration (NOAA), have allowed to retrieve temperature and moisture  
103 profiles with a vertical resolution of about 3 to 5 km in the troposphere, as defined by the  
104 instrumental weighting functions (e.g. *Susskind et al., 1984; Chedin et al., 1985*). A new  
105 generation of instruments has been launched on polar platforms satellites, such as

106 Interferometric Monitor for Greenhouse gases (IMG, e.g. Ogawa et al., 1994; Clerbaux et al.,  
107 1998), Tropospheric Emission Spectrometer (TES, e.g. Shephard et al., 2008; Worden et al.,  
108 2012), the Advanced Infrared Sounder (AIRS, Chahine et al., 1990; Aumann and Miller,  
109 1995), and the Infrared Atmospheric Sounding Interferometer (IASI, e.g. Clerbaux et al.,  
110 2009; Hilton et al., 2012). Thanks to a larger number of spectral channels and an enhanced  
111 spectral resolution, these instruments lead to improved vertical resolutions down to 1 km and  
112 higher precision of both the atmospheric temperature and water vapor content retrieval.

113 We will focus our study on the reliability of the water vapor mixing ratio (WVMR) vertical  
114 profiles retrieved from the IASI spectrometer, which has been launched onboard the polar  
115 orbiting meteorological satellites MetOp (Meteorological Operational), which forms the space  
116 segment of the overall EUMETSAT Polar System (EPS).

117 Main mission of IASI is the operational meteorology (e.g. Zhou et al., 2009), although air-  
118 composition and climate applications are also well covered by the instrument as also  
119 discussed before launch (e.g. Chazette et al., 1998; Clerbaux et al., 1998) and now  
120 demonstrated (e.g. Crevoisier et al., 2013a; Griffin et al., 2013; Grieco et al., 2013). Hereafter  
121 we will only discuss the comparison between IASI-derived WVMR and the simultaneous  
122 measurements performed by a H<sub>2</sub>O-Raman lidar deployed on the Balearic Island of Menorca  
123 | in the framework of the Hydrological cycle in the Mediterranean eXperiment (HyMeX,  
124 <http://www.hymex.org/>, Chazette et al., 2013) and Chemistry-Aerosol Mediterranean  
125 Experiment (ChArMEx, <http://www.mistrals-home.org>).

126 For our concern, the IASI-derived WVMR operational Level-2 products have been available  
127 via the European Organisation for the Exploitation of Meteorological Satellites  
128 (EUMETSAT) for several years. In particular, vertical profiles of WVMR measurements are  
129 retrieved from infrared radiances at the global scale (e.g. Carissimo et al., 2005; Schlüssel et

130 *al.*, 2005; *Schneider and Hase*, 2011). The robustness of such products has to be checked, and  
131 the field experiments that were held during the HyMeX and ChArMEx international programs  
132 are a very good opportunity for that purpose. Few validation exercises have been conducted  
133 on the WVMR operational product. The main reason seems that for meteorological  
134 forecasting, the radiances are directly assimilated in the models (e.g. *Hilton et al.*, 2009;  
135 *Hilton et al.*, 2012; *Heilliette*, 2013; *Matricardi and McNally*, 2013; *Xu et al.*, 2013).  
136 Nevertheless, the WVMR Level-2 product could have a great interest in order to help field  
137 experiment analyses. Moreover, few validations are available in the scientific literature.  
138 *Pougatchev et al.* (2009) used rawindsounding measurements to assess the error covariance  
139 matrix needed for the inversion algorithm. *Masiello et al.*, (2013) argue that lidar  
140 measurements are excellent candidates for the validation of spaceborne sensors. They used  
141 different measurement techniques during the Convective and Orographically-induced  
142 Precipitation Study (COPS) campaign, and the comparisons were performed with a limited  
143 number of lidar profiles (6) during the same season. Such validations are very delicate  
144 because performing atmospheric measurements of WVMR with the required accuracy for  
145 satellite retrieval validation is a challenging issue due to the high spatio-temporal variability  
146 of atmospheric water vapor. The spatiotemporal coincidence between the ground-based and  
147 the spaceborne measurements has to be guaranteed to avoid important sampling errors.

148 In the following section, the Raman lidar system used for IASI WVMR comparisons and its  
149 technical specifications will be presented as well as the experimental sites used to conduct the  
150 validation during the Mediterranean project. The IASI derived WVMR product specifications  
151 will also be introduced. The third section will present the experimental comparisons. The  
152 statistical tools used to evaluate the WVMR products will be introduced and the experimental  
153 results obtained will be presented. Then, the influence of both the air mass origin and their

154 | aerosol content in the results will be discussed. Finally, the main results will be summarized  
155 | in the conclusion.

## 156 | 2 Observations

157 | The comparison between the WVMR ground-based lidar measurements and the IASI  
158 | operational products took place in the framework of both HyMeX and ChArMEx Special  
159 | Observation Periods during September-October 2012 and June-July 2013, respectively, on the  
160 | Balearic island of Menorca. During HyMeX/IODA-MED (Innovative Observing and Data  
161 | Assimilation systems for the MEDiterranean Weather), the Water vapor and Aerosol lidar  
162 | (WALI) was located close to La Ciutadella (Western part of the island, 39°60'00" N and  
163 | 3°50'20"E), while during ChArMEx it was deployed close to Mahon (Eastern part of the  
164 | island, 39°53'12" N and 4°15'31" E). Hence, the WVMR vertical profiles derived from the  
165 | IASI spaceborne spectrometer (Ether CNES/CNRS-INSU Ether web site <http://www.pole-ether.fr>)  
166 | have been compared to the ones measured by WALI during nighttime for field  
167 | experiment durations of 6 and 3 weeks for HyMeX and ChArMEx, respectively. The use of  
168 | the Raman technique limits the range of daytime measurements (< 1 km), which are  
169 | consequently not relevant for a validation purpose in the lower and middle troposphere.

### 170 | 2.1 The WALI Raman lidar

171 | The WALI instrument uses an emitting wavelength of 354.7 nm and is designed to fulfill eye-  
172 | safe conditions (Table 1). The instrument, its calibration and the associated errors are  
173 | documented in *Chazette et al. (2013)* and will not be detailed here. During all the experiment  
174 | the acquisition was performed for mean profiles of 1000 laser shots leading to a temporal  
175 | sampling close to 1 minute. The UV pulse energy is ~60 mJ and the pulse repetition  
176 | frequency is 20 Hz. It is equipped with four detection channels: an aerosol board including  
177 | co-polarized and cross polarized channels with respect to the laser emission, a channel

178 dedicated to the detection of the water vapor Raman signal at 407.5 nm and a fourth channel  
179 dedicated to the recording of the atmospheric nitrogen Raman signal at 386.6 nm.

180 The design of the WALI system leads to very good capabilities in terms of low altitude  
181 overlap and WVMR retrieval during nighttime. The absolute deviation from rawindsoundings  
182 is less than 0.5 g/kg (*Chazette et al.*, 2013). The error on the WVMR reaches 11% in the  
183 marine boundary layer and decreases to 7% below 5 km range for a temporal averaging of 20  
184 minutes and a vertical resolution of 15 m. Precision can deteriorate very quickly thereafter  
185 due to the decreasing Signal to Noise Ratio (SNR) with altitude. It is also worse during  
186 daytime, but measurements can be performed with the same uncertainty for altitude ranges  
187 below 1 km using a temporal averaging over ~1 hour. For the inter-comparisons presented in  
188 this paper, the chosen averaging time is 30 minutes, centered on the time value of the IASI  
189 profile to be compared, and the altitude range is from 0.3 to 7 km above the mean sea level  
190 (amsl). The original vertical and temporal resolutions are 15 m and 1 minute, respectively.  
191 The lidar profiles were smoothed for the comparison so that the vertical resolution used for  
192 this study is ~41 m.

## 193 2.2 The MetOp /IASI satellite data

194 MetOp (Meteorological Operational) consists of a series of three polar heliosynchronous  
195 orbiting satellites, to be flown successively for more than 14 years, from 2006. This series  
196 forms the space segment of the overall EUMETSAT Polar System (EPS). EPS is the  
197 European contribution to the Initial Joint Polar System agreement (IJPS), an agreement  
198 between EUMETSAT and NOAA. MetOp flies in a Low Earth orbit at an altitude of 817 km  
199 corresponding to local 'morning', while the US is responsible for 'afternoon' coverage (*Klaes  
200 et al.*, 2007). MetOp-A (launched on 19 October 2006) and MetOp-B (launched on 17  
201 September 2012) provide detailed observations of the global atmosphere, oceans and



202 continents. MetOp-C is due to be launched in 2017. The series provides data for both  
203 operational meteorology and climate studies. A combination of passive remote sensing  
204 instruments offers the capability to observe the Earth by day and night, as well as under  
205 cloudy conditions. The most innovative and one of the key instruments on MetOp is the  
206 Michelson interferometer IASI. Three IASI instruments were developed for MetOp by CNES  
207 (Centre National d'Etudes Spatiales) in cooperation with EUMETSAT. They are built to  
208 provide temperature and moisture measurements with unprecedented accuracy and resolution,  
209 and additionally to provide information for the monitoring of atmospheric trace gases.

210 The bandwidth of IASI is divided into 8461 spectral channels between 645 and 2760  $\text{cm}^{-1}$  with  
211 a mean spectral resolution of 0.5  $\text{cm}^{-1}$  after apodization. IASI scans across-track in 30  
212 successive elementary fields of view (EFOV), each composed of 4 instantaneous fields of  
213 view (IFOV) of  $0.8225^\circ$  leading to a footprint of 12 km diameter at sub-satellite point. The  
214 footprint dimension increases from 20 to 39 km along-track directions to the swath edge,  
215 respectively (Cayla, 1993). The swath width on the ground is approximately 2200 km, which  
216 provides global Earth coverage twice per day.

217 Operational products from EPS/MetOp are generated in the EPS Core Ground Segment. The  
218 IASI Level-2 processing development targeted the generation of temperature and humidity  
219 profile information, the associated surface information and the retrieval of some trace gas  
220 species: CO, O<sub>3</sub>, CH<sub>4</sub>, N<sub>2</sub>O and CO<sub>2</sub>. The vertical temperature and water-vapor profiles are  
221 currently distributed on a 90-level grid extending between 0.005 and 1050 hPa (August *et al.*,  
222 2012). Note that the operational product uses a statistical approach to retrieve the geophysical  
223 parameters. Other approaches use a physical scheme and give access to a better vertical  
224 resolution (e.g. Amato *et al.*, 2009; Masiello *et al.*, 2013). Nevertheless, the goal of this paper

225 is to provide quantitative elements of validation for the operational product using the  
226 statistical approach.

227 Both the temperature and moisture of the troposphere and lower stratosphere are derived  
228 under cloud-free conditions with a vertical resolution of 1-2 km in the lower troposphere; a  
229 horizontal resolution of 25 km, and an accuracy of 1 K and 10%, respectively. The number of  
230 independent pieces of information which are determined in the moisture profiles is in the  
231 order of 10. The sensitivity to the lower troposphere is lower and leads to larger error beneath  
232 3 km, although ~80% of moisture is contained in this layer. For the WVMR retrieval, the  
233 IASI weighting functions are generally maximum above 700 hPa.

234 For the comparison presented hereafter, we considered the 12 closest IASI pixels from the  
235 lidar ground-based station. The mean values and the associated standard deviations are then  
236 calculated if the number of relevant IASI-derived WVMR profiles are at least equal to 6.

### 237 3 Comparison between the IASI and WALI water vapor products

238 Here we assess the representativeness of IASI in terms of atmospheric moisture content  
239 considering both vertical profiles and integrated values to evaluate the potentiality of these  
240 products to be used for meteorological studies purposes. The relevant IASI coincidences are  
241 established before a comparison with the Raman lidar WALI separately for the two time  
242 periods of field experiments.

#### 243 3.1 Coincidences

244 Figure 1 gives the temporal evolution of the WVMR vertical profiles above Menorca during  
245 the two time periods on which field experiments were conducted. The water vapor contents  
246 are highly variable and highlight contrasted atmospheric situations, which are of interest for  
247 comparison to IASI-derived WVMR. On the same figure are given the satellite overpass times  
248 for which comparisons are relevant. We have identified 30 coincidences in cloud-free

249 conditions with available IASI profiles, during September-October 2012 and June-July 2013.  
 250 Note that the presence of high aerosol content is also classified as a cloudy condition. For  
 251 each time period, the coincidences are identified by their number in a chronological way  
 252 hereafter called coincidence number (CN). All the coincidences are reported in Table 2 and  
 253 Table 3 for the time periods of HyMeX and ChArMEx, respectively (15 CN each). The  
 254 distance between the central pixel of IASI and the lidar ground-based station ( $D$ ), and the  
 255 number of relevant IASI pixels ( $N$ ) are also indicated.

### 256 3.2 WVMR vertical profiles

257 The WVMR vertical profiles for the whole retained atmospheric situations are shown in  
 258 Figure 2 and Figure 3 for HyMeX and ChArMEx, respectively. The coincident WVMR  
 259 simulated from the European Centre for Medium-Range Weather Forecasts (ECMWF)  
 260 operational analysis are also plotted on the figures. The 9 closest model grids from the  
 261 ground-based lidar station are considered to compute both the mean and the standard  
 262 deviation vertical profiles. The meteorological fields have been provided by ECMWF and  
 263 have been obtained from the ESPRI/IPSL data server for a horizontal resolution of  $0.5^\circ$ .

264 The statistical indicators used to evaluate the relevance of the IASI-derived WVMR ( $r_{iasi}$ )  
 265 with respect to lidar observations ( $r_{lidar}$ ) are the Root Mean Square Error (RMSE) and the  
 266 (Pearson) correlation (COR). They are often used to evaluate model performances as in  
 267 *Boylan and Russell (2006)* and can be written as

$$268 \quad RMSE = \sqrt{\frac{1}{N_t} \sum_{i=1}^{N_t} (r_{iasi} - r_{lidar})^2} \quad (1)$$

$$269 \quad COR = \frac{\sum_{i=1}^{N_t} (r_{lidar} - \bar{r}_{lidar})(r_{iasi} - \bar{r}_{iasi})}{\sqrt{\sum_{i=1}^{N_t} (r_{lidar} - \bar{r}_{lidar})^2 \sum_{i=1}^{N_t} (r_{iasi} - \bar{r}_{iasi})^2}} \quad (2)$$

270 where  $N_t$  is the total number of coincidences and the overbar terms are averages. The vertical  
271 values for both  $r_{IASI}$  and  $r_{lidar}$  are used at the IASI-L2 pressure level grid.

272 Figure 4 gives the vertical profiles of both RMSE and COR for the two time periods. The  
273 statistical indicators have been computed between WALI and IASI, and WALI and ECMWF  
274 data.

275 During the first time period (fall time), the lidar and modelled profiles are in better agreement  
276 with a mean RMSE and COR of 0.42 g/kg and 77% (between 0.5 and 7 km), respectively,  
277 whereas between the lidar and IASI vertical profiles these values reach ~0.6 g/kg and 70%,  
278 respectively. The shapes of RMSE and COR against altitude are however very similar. It is  
279 not surprising because ECMWF analyses are made by assimilating the IASI radiances (e.g.  
280 *Hilton et al.*, 2012) in addition to the rawinsounding performed in Palma de Mallorca (100 km  
281 Southwest of Menorca). In the planetary boundary layer (PBL) more discrepancy could be  
282 encountered due to local effects.

283 An opposite behavior happens in terms of RMSE for the second time period (summer time)  
284 where the IASI-derived WVMR ( $RMSE = 1.64$  g/kg) is better than that of the model  
285 ( $RMSE = 2.04$  g/kg) when compared to the Raman lidar. It is mainly true below 2 km.  
286 Nevertheless, the correlation is better between the lidar and the ECMWF analyses (0.82) than  
287 between the lidar and IASI (0.59).

288 In the free troposphere, where the IASI weighted functions mostly have their maxima, the  
289 agreement is better according to the **RMSE and COR** indicators. This agreement is higher for  
290 the HyMeX time period and might be due to a lesser influence of the aerosol layers. For this  
291 period  $RMSE$  is lower than 0.5 g/kg and  $COR$  is ~77%, to be compared to ~1.1 g/kg and  
292 ~72% during the ChArMEx time periods. Below 2 km, the agreement is degraded as  
293 expected:  $RMSE$  is between ~2 and 3 g/kg and the  $COR$  value tends to 0. Table 4 summarizes

294 the results for different atmospheric layers between 0.5 and 7 km. Such results are consistent  
295 with those of *Schneider and Hase* (2011) who used rawinsoundings as validation tools for the  
296 IASI WVMR Level-2 operational products. With the exception of the PBL, they found a  
297 correlation coefficient of  $\sim 0.80$ .

### 298 3.3 Water vapor integrated content

299 When considering the Water vapor integrated content (WVIC) between 0.5 and 7 km, the  
300 agreement between lidar- and IASI-derived moisture is within a standard deviation between  
301 0.18 and 0.25  $\text{g}/\text{cm}^2$ . Figure 5 illustrates this agreement: the IASI-derived WVIC exhibits a  
302 bias lower than 0.15  $\text{g}/\text{cm}^2$  compared to the one retrieved from WALI. In fact, the WVIC  
303 retrieved from IASI is in the range value (between 0.5 and 2  $\text{g}/\text{cm}^2$ ) for the HyMeX time  
304 period (fall 2012), but it is mostly underestimated by  $\sim 10\%$  during the ChArMEx time period  
305 (summer 2013). The slopes of the regressions are 0.89 and 0.81 for the HyMeX and  
306 ChArMEx time periods, respectively. Note that during the HyMeX time period (fall 2012),  
307 the agreement between the lidar and IASI profiles is better, even in the general shape.

308 When compared to ECMWF analyses, standard deviations with respect to WALI are close to  
309 0.17 and 0.45  $\text{g}/\text{cm}^2$  for the two previous time periods, respectively. With respect to previous  
310 IASI cross-comparisons, results are not degraded during the HyMeX fall period but  
311 significantly worse over the ChArMEx summer period where the slope of the linear fit is  
312 close to 0.70. Such discrepancy (underestimation) may be due to an incorrect consideration of  
313 the instrumental error in the variance/covariance matrix needed for the assimilation process  
314 (e.g. *Wang et al.*, 2013). The error on the contribution to the IASI radiances may be linked to  
315 local heating associated to the aerosol presence not being taken into account in the model, as  
316 for all spaceborne infrared sensors (e.g. *Pierangélo et al.*, 2004). This point is not within the  
317 topic of this paper and has to be further investigated.

#### 318 4 Influence of the air mass origins - aerosol as air mass tracer

319 Among all 30 coincidences, the origins of air masses are very different and can be  
320 characterized using simultaneously several aerosol optical properties and air mass back  
321 trajectories. The Raman lidar WALI offers the capability to retrieve fundamental aerosol  
322 optical properties (*Chazette et al.*, 2013): the vertical profiles of the volume depolarization  
323 ratio (VDR) to identify the presence of dust-like aerosols, the aerosol extinction coefficient  
324 (AE) to locate in altitude the scattering layers, the equivalent backscatter to extinction ratio  
325 (BER) which is proportional to the single scattering albedo, and the aerosol optical thickness  
326 (AOT) characterizing the aerosol column burden. The inversion process used both the N<sub>2</sub>-  
327 Raman and elastic channels at 355 nm and is described in various papers as *Royer et al.*  
328 (2011) or *Chazette et al.* (2012) where the related uncertainties are assessed. Hence, using the  
329 aerosol optical properties described above, coupled with air mass back trajectory analysis, the  
330 air masses influencing the IASI-derived WVMR can be identified.

##### 331 4.1 Aerosol optical properties

332 As in Figure 1, the dates of the relevant IASI coincidences are highlighted in white dotted  
333 lines in Figure 6. This figure represents the temporal evolution of the vertical profile of VDR  
334 for HyMeX and ChArMEX time periods, respectively. In general, the relevant coincidences do  
335 not occur during the major dust events where the VDR is maximal (in brown on the figure),  
336 likely because the dust plume is classified as cloud: it is sufficiently thick to significantly  
337 influence the brightness temperature used to **invert** the IASI infrared spectrum. Nevertheless,  
338 other sources of aerosol may affect the IASI measurements. Thereby, the BER is also an  
339 important parameter to identify the aerosol types (e.g. *Catrrall et al.*, 2005) as it is linked to  
340 their chemical composition. It is given in Figure 7 as a column average and presents a strong  
341 variability, ranging from  $\sim 0.01 \text{ sr}^{-1}$  for pollution aerosol (e.g. *Raut and Chazette*, 2009) to  
342  $\sim 0.04 \text{ sr}^{-1}$  for marine aerosol (e.g. *Flamant et al.*, 2000). The intermediate values are for

343 aerosol mixing, dust aerosols (e.g. *Mattis et al.*, 2002; *Chazette et al.*, 2007) or long-range  
344 transport pollution aerosols (e.g. *Chazette et al.*, 2012). The AE and VDR vertical profiles are  
345 also given Figure 8 and Figure 9 for the coincidences of the two time periods. They often  
346 show strong heterogeneities with respect to altitude which are directly related to the vertical  
347 profiles of WVMR given Figure 2 and Figure 3, respectively. All the vertical structures  
348 encountered have to be investigated to compare the WVMR-derived from IASI and WALI.  
349 The aerosol atmospheric content in terms of AOT is also very different from one observation  
350 to another because it ranges from 0.04 (very clean air) to ~0.4 (polluted air and/or dust event).  
351 Hence, the coincidences are very diverse for an inter-comparison exercise, and allow  
352 evaluating the IASI-derived WVMR retrieval for very distinct atmospheric situations and  
353 aerosol contents.

#### 354 4.2 Air mass back trajectories

355 Air mass back trajectories have been computed to determine the corresponding aerosol  
356 transport routes using the NOAA Hybrid Single Particle Lagrangian Integrated Trajectory  
357 (HYSPLIT) model (*Draxler and Rolph*, 2003) with 3-hourly archived meteorological data  
358 provided from the US National Centers for Environmental Prediction (NCEP) Global Data  
359 Assimilation System (GDAS) at the horizontal resolution of  $0.5^\circ$ . The altitudes of the  
360 trajectory starting points (1, 2 and 4 km) were selected primarily from the lidar observations  
361 of aerosol layer heights highlighted in Figure 8 and Figure 9. The air mass back trajectories  
362 are shown Figure 10, Figure 11 and Figure 12 for the 3 starting points and for each time  
363 period. One path was drawn on 72 hours for each coincidence between IASI and WALI  
364 measurements. The air mass origins are very variable during the time periods for all starting  
365 point altitudes. There are two major contributions to the air masses passing over Menorca, the  
366 first one from the Sahara and the second one from the Atlantic Ocean.

### 367 4.3 Discussion

368 The summary of our conclusion about the origins of air mass revealed by the shape of the  
369 WVMR vertical profile is given in Table 2 and Table 3 for the HyMeX and ChArMEx time  
370 periods, respectively. Depolarizing layers (DL) and residual pollution layers (RPL) are  
371 specifically identified.

372 The atmospheric situations observed during the coincidences present significantly high  
373 moisture content ( $WVMR > 5 \text{ g/kg}$  in the free troposphere and  $WVIC$  close to  $2 \text{ g/cm}^2$ ) for 4  
374 (5) cases during the HyMeX (ChArMEx) time period, which correspond to  $CN = 1, 2, 6$  and  
375 10 (2, 5, 6, 7 and 8). Such situations are generally well represented by the Level-2 product of  
376 the IASI operational ground segment, excepted for  $CN = 10$  during the HyMeX time period  
377 where the IASI product overestimates the WVMR by  $\sim 25\%$ . In this case, the air mass came  
378 from Morocco and brought moisture with dust aerosols between ground and  $\sim 4 \text{ km}$  above the  
379 mean sea level (amsl). Nevertheless, it must be noted that Saharan air masses are often  
380 associated with higher moisture content and the agreement between IASI- and WALI-derived  
381 WVMR is generally better for these air masses because of the smoother transitions in vertical  
382 structures due to higher moisture content in these layers.

383 The major discrepancies are observed for the drier air masses ( $WVIC$  less or close to  $1 \text{ g/cm}^2$ )  
384 which present a strong vertical gradient of WVMR, generally between the PBL and the free  
385 troposphere. Such a gradient is not reproduced from IASI measurements due to its insufficient  
386 vertical resolution. Note that the dry air masses observed during the field campaigns  
387 originated from the Atlantic and had a small AOT ( $< 0.2$ ).

388 For the other coincidences, the agreement between IASI and WALI is good. The median  
389 value of the atmospheric aerosol content ( $AOT \sim 0.2$ ) is similar during the two time periods  
390 and cannot explain the observed differences between them. During the ChArMEx time period



391 several coincidences are associated with very clean air ( $AOT < 0.1$ ) situations. Furthermore,  
392 the differences observed in the WALI/ECMWF comparison cannot be explained by the  
393 presence of an aerosol layer. These discrepancies seem linked to a seasonal role, which could  
394 be due to an incorrect consideration of the sea surface temperature in the model.

395 The air mass origin plays a major role through the shape of the original vertical structure  
396 which can be kept during several days along the transport. As discussed by *Kim et al.* (2004),  
397 the larger amount of water vapor in an aerosol layer contributes to a higher radiative heating,  
398 increasing the potential temperature and static stability of the layer. This may help to maintain  
399 the structure of the layer for a longer period of time. Note that the vertical structures observed  
400 during our two field campaigns are not uncommon in the atmosphere (e.g. *Chazette et al.*,  
401 2001; *Kim et al.*, 2009). All this suggests a need for an increased vertical resolution of  
402 infrared spaceborne sounders, and then for the improvement of their spectral resolution (e.g.  
403 *Crevoisier et al.*, 2013b).

## 404 5 Conclusion

405 | Following the international field campaigns HyMeX (Hydrological cycle in the  
406 | Mediterranean eXperiment) and ChArMEx (Chemistry-Aerosol Mediterranean Experiment)  
407 | in fall 2012 and summer 2013, respectively, 30 relevant coincidences between the ground-  
408 | based lidar WALI (Water vapor and Aerosol lidar) and the spaceborne instrument Infrared  
409 | Atmospheric Sounding Interferometer (IASI) have been selected to conduct a comparison  
410 | exercise of the water vapor mixing ratio (WVMR) vertical profile retrieval. The general result  
411 | is in good agreement between the two instruments. Two statistical indicators generally used to  
412 | evaluate model performances have been considered: the Root Mean Square Error (RMSE)  
413 | and the (Pearson) correlation (COR). In the middle troposphere (2-7 km amsl) the COR value  
414 | is ~77 and 72%, and the RMSE is lower than 0.5 and 1.1 g/kg for the fall and summer

415 | periods, respectively. Discrepancies are higher in the **planetary boundary layer (PBL)** because  
416 | the weighted functions of IASI do not correctly sample this layer close to the ground  
417 | (*RMSE* ~ 1.6 g/kg and *COR* < 0.4). Considering the water vapor integrated content within the  
418 | altitude range of 0.3 and 7 km amsl, the standard deviation between IASI and WALI are 0.18  
419 | and 0.25 g/cm<sup>2</sup> for the fall and summer periods, respectively. The disagreement is higher  
420 | during summer time and we may suspect the presence of aerosol layers and/or contrasted  
421 | vertical atmospheric structures to be responsible for this bias.

422 | During coincidences, we note that the integrated atmospheric aerosol content has been found  
423 | with aerosol optical thickness between 0.04 and 0.4 associated with various particle types  
424 | (pollution, marine or dust aerosols), as identified from both the lidar-derived backscatter to  
425 | extinction ratio and air mass back trajectories. The aerosol optical thickness does not  
426 | significantly affect the results of the intercomparison. The divergence on the WVMR vertical  
427 | profile is mainly due to the existence of sharp transitions which mainly occurs between the  
428 | PBL and the free troposphere. The agreement is generally better for Saharan air masses  
429 | because of the smoother transitions in vertical structures due to higher moisture content in  
430 | these layers (~5 g/kg). Our results calls for an improvement of the spectral resolution of the  
431 | Fourier transform spectrometer IASI. Such consideration is being studied for the next  
432 | generation, the so-called IASI-NG. Moreover, the synergetic use of microwave measurements  
433 | is capable of improving the water vapor retrievals, especially in the PBL. An upcoming  
434 | version (6) of the operational IASI **Level-2** processor with synergistic use of the Advanced  
435 | Microwave Sounding Unit (AMSU) and the Microwave Humidity Sounder (MHS) data is  
436 | scheduled. It was reported **at the last International TOVS Study Conference hold to Jeju**  
437 | **Island (South Korea, 26 March - 1 April 2014)** to contain substantial improvements of the  
438 | profiles when compared with **the European Centre for Medium-Range Weather Forecasts**  
439 | **(ECMWF)** analysis, in particular in the lower levels and for the entire water vapor profiles.

440 The approach presented in this study can be applied to the next generation of IASI operational  
441 water vapor products.

442 **Acknowledgments.** This work was supported by the French Agence Nationale de la  
443 Recherche (ANR) via the HyMeX /IODA-MED project, the French space agency (CNES) and  
444 the Commissariat à l'Energie Atomique (CEA). We also thank M. Sicard and F. Dulac for  
445 their help for installing the lidar station on the Menorca Island. ECMWF data used in this  
446 study have been obtained from the ECMWF Data Server. The authors would additionally like  
447 to thank the HyMeX and ChArMEx programs for their support. The IASI Level-2 Water  
448 Vapor Mixing Ratio profiles used in this paper are Courtesy Ether CNES/CNRS-INSU Ether  
449 web site <http://www.pole-ether.fr>.

450 6 References

- 451 Amato, U., Antoniadis, A., De Feis, I., Masiello, G., Matricardi, M., and Serio, C.: Technical  
452 Note: Functional sliced inverse regression to infer temperature, water vapour and ozone  
453 from IASI data, *Atmos. Chem. Phys.*, *9*, 5321-5330, doi:10.5194/acp-9-5321-2009, 2009.
- 454 Aumann, H.H., and Miller, C.: Atmospheric Infrared Sounder (AIRS) on the Earth Observing  
455 System, in *Advanced and next-generation satellite*, H. Fujisada and M.N. Sweeting, eds.,  
456 Proc. SPIE 2583, 332-338, 1995.
- 457 August, T., Klaes, D., Schlüssel, P., Hultberg, T., Crapeau, M., Arriaga, A., O'Carroll, A.,  
458 Coppens, D., Munro, R., and Calbet, X.: IASI on Metop-A:Operational Level 2 retrievals  
459 after five years in orbit, *Journal of Quantitative Spectroscopy & Radiative Transfer*, *113*,  
460 1340–1371, 2012.
- 461 Bormann, N., Collard, A., and Bauer, P.: Estimates of spatial and interchannel observation-  
462 error characteristics for current sounder radiances for numerical weather prediction. II:  
463 Application to AIRS and IASI data, *Q. J. Roy. Meteorol. Soc.*, *136*, 1051-1063, 2010.
- 464 Boylan, J. W. and Russell, A. G.: PM and light extinction model performance metrics, goals,  
465 and criteria for three-dimensional air quality models, *Atmos. Environ.*, *40*, 4946–4959,  
466 2006.
- 467 Carissimo, A., De Feisi, I., and Serio, C.: The physical retrieval methodology for IASI: the -  
468 IASI code, *Environ. Modell. Softw.*, *20*, 9, 1111–1126, doi:10.1016/j.envsoft.2004.07.003,  
469 2005.
- 470 Catrall, C., Reagan, J., Thome, K., and Dubovik, O.: Variability of aerosol and spectral lidar  
471 and backscatter and extinction ratios of key aerosol types derived from selected Aerosol  
472 Robotic Network locations, *J. Geophys. Res.*, *110*, D10S11, doi:10.1029/2004JD005124,  
473 2005.
- 474 Cayla, F-R.: IASI infrared interferometer for operations and research. In: Chedin A, Chahine  
475 MT, Scott NA, editors. *High spectral resolution infrared remote sensing for Earth's*  
476 *weather and climate studies*, NATO ASI series, vol. I 9. Berlin: Springer Verlag, 1993.
- 477 Chahine, M.T., O'Callaghan, F.G., Aumann, H.H., Capps, R.W., Haskins, R.D., Pagano, R.J.,  
478 and Schindler, R.A.: *Atmospheric Infrared Sounder (AIRS)-Science and measurement*  
479 *requirements*, NASA-TM-104977, Washington D.C., 36 pp, 1990.
- 480 Chazette, P., Clerbaux, C., and Mégie, G.: Radiative forcing of methane estimated using nadir  
481 spectral radiances, *Appl. Opt.*, *37*, 15, 3113-3120, 1998.
- 482 Chazette, P., Pelon, J., Moulin, C., Dulac, F., Carrasco, I., Guelle, W., Bousquet, P., and  
483 Flamant, P.H.: Airborne lidar and Meteosat synergy to characterize a Saharan dust plume  
484 over the Azores during SOFIA/ASTEX, *Atmos. Environ.*, *35*, 4297-4304, 2001.

- 485 Chazette, P., Sanak, J., and Dulac, F.: New Approach for Aerosol Profiling with a lidar  
486 Onboard an Ultralight Aircraft: Application to the African Monsoon Multidisciplinary  
487 Analysis, *Environ. Sci. Technol.*, *41*, 8335–8341, 2007.
- 488 Chazette, P., Bocquet, M., Royer, P., Winiarek, V., Raut, J.-C., Labazuy, P., Gouhier,  
489 M., Lardier, M., and Cariou, J.-P.: Eyjafjallajökull ash concentrations derived from both  
490 lidar and modeling, *J. Geophys. Res.*, *117*, D00U14, doi:10.1029/2011JD015755, 2012.
- 491 Chazette, P., Marnas, F., and Totems, J.: The mobile Water vapor Aerosol Raman lidar and  
492 its implication in the frame of the HyMeX and ChArMEx programs: application to a dust  
493 transport process, *Atmos. Meas. Tech. Discuss.*, *6*, 10653-10698, doi:10.5194/amtd-6-  
494 10653-2013, 2013.
- 495 Chedin, A., Scott, N. A., Wahiche, C., and Moulinier, P.: The improved initialization  
496 inversion method: a high resolution physical method fo temperature retrievals from  
497 satellites of the TIROS-N series, *J. Climate Appl. Meteorol.*, *24*, doi:10.1175/1520-  
498 0450(1985)024, 128:143, 1985.
- 499 Clerbaux, C., Chazette, P., Hadji-Lazaro, J., Müller, J.F., Clough, T., and Mégie, G.: Remote  
500 sensing of O<sub>3</sub>, CO and CH<sub>4</sub> using a spaceborne nadir-viewing instrument, *J. Geophys. Res.*,  
501 *103*, D15, 18999-19013, 1998.
- 502 Clerbaux, C., Boynard, A., Clarisse, L., George, M., Hadji-Lazaro, J., Herbin, H., Hurtmans,  
503 D., Pommier, M., Razavi, A., Turquety, S., Wespes, C., and Coheur, P.-F.: Monitoring of  
504 atmospheric composition using the thermal infrared IASI/MetOp sounder, *Atmos. Chem.*  
505 *Phys.*, *9*, 6041–6054, doi:10.5194/acp-9-6041-2009, 2009.
- 506 Collard, A.D., and McNally, A.P.: The assimilation of Infrared Atmospheric Sounding  
507 Interferometer radiances at ECMWF, *Q. J. Roy. Meteorol. Soc.*, *135*, 1044-1058, 2009.
- 508 Crevoisier, C., Nobileau, D., Armante, R., Crépeau, L., Machida, T., Sawa, Y., Matsueda, H.,  
509 Schuck, T., Thonat, T., Pernin, J., Scott, N. A., and Chédin, A.: The 2007–2011 evolution  
510 of tropical methane in the mid-troposphere as seen from space by MetOp-A/IASI, *Atmos.*  
511 *Chem. Phys.*, *13*, 4279-4289, doi:10.5194/acp-13-4279-2013, 2013a.
- 512 Crevoisier, C., Clerbaux, C., Guidard, V., Phulpin, T., Armante, R., Barret, B., Camy-  
513 Peyret, C., Chaboureaud, J.-P., Coheur, P.-F., Crépeau, L., Dufour, G., Labonnote, L.,  
514 Lavanant, L., Hadji-Lazaro, J., Herbin, H., Jacquinet-Husson, N., Payan, S., Péquignot, E.,  
515 Pierangelo, C., Sellitto, P., and Stubenrauch, C.: Towards IASI-New Generation (IASI-  
516 NG): impact of improved spectral resolution and radiometric noise on the retrieval of  
517 thermodynamic, chemistry and climate variables, *Atmos. Meas. Tech. Discuss.*, *6*, 11215-  
518 11277, doi:10.5194/amtd-6-11215-2013, 2013b.
- 519 Draxler, R.R., and Rolph, G.D.: HYSPLIT (HYbrid Single-Particle Lagrangian Integrated  
520 Trajectory) Model access via NOAA ARL READY Website

521 (<http://www.arl.noaa.gov/ready/hysplit4.html>). NOAA Air Resources Laboratory, Silver  
522 Spring, MD, 2003.

523 Flamant C., Pelon, J., Chazette, P., Trouillet, V., Quinn, P., Frouin, R., Bruneau, D., Léon,  
524 J.F., Bates, T., Johnson, J., and Livingston, J.: Airborne lidar measurements of aerosol  
525 spatial distribution and optical properties over the Atlantic Ocean during an European  
526 pollution outbreak of ACE-2, *Tellus*, 52B, 662-667, 2000.

527 Grieco, G., Masiello, G., Matricardi, M., and Serio, C.: Partially scanned interferogram  
528 methodology applied to IASI for the retrieval of CO, CO<sub>2</sub>, CH<sub>4</sub> and N<sub>2</sub>O, *Opt. Express*,  
529 21, 24753-24769; doi: 10.1364/OE.21.024753, 2013.

530 Griffin, D., Walker, K. A., Franklin, J. E., Parrington, M., Whaley, C., Hopper, J.,  
531 Drummond, J. R., Palmer, P. I., Strong, K., Duck, T. J., Abboud, I., Bernath, P. F.,  
532 Clerbaux, C., Coheur, P.-F., Curry, K. R., Dan, L., Hyer, E., Kliever, J., Lesins, G.,  
533 Maurice, M., Saha, A., Tereszchuk, K., and Weaver, D.: Investigation of CO, C<sub>2</sub>H<sub>6</sub> and  
534 aerosols in a boreal fire plume over eastern Canada during BORTAS 2011 using ground-  
535 and satellite-based observations and model simulations, *Atmos. Chem. Phys.*, 13, 10227-  
536 10241, doi:10.5194/acp-13-10227-2013, 2013.

537 Heilliette S., Y. J. Rochon, L. Garand, and J. W. Kaminski: Assimilation of Infrared  
538 Radiances in the Context of Observing System Simulation Experiments  
539 *Journal of Applied Meteorology and Climatology*, 52(4), 1031-1045, doi:10.1175/JAMC-  
540 D-12-0124.1, 2013.

541 Held, I.M., and Soden, B.J.: Water vapor feedback and global warming, *Annual Rev. Energy*  
542 *Environ.*, 25, 441-475, DOI: 10.1146/annurev.energy.25.1.441, 2000.

543 Hilton, F., Atkinson, N.C., English, S.J., and Eyre, J.R.: Assimilation of IASI at the Met  
544 Office and assessment of its impact through observing system experiments, *Q. J. Roy.*  
545 *Meteorol. Soc.*, 135, 495-505, 2009.

546 Hilton, F., Armante, R., August, T., Barnet, C., Bouchard, A., Camy-Peyret, C., Capelle, V.,  
547 Clarisse, L., Clerbaux, C., Coheur, P.-F., Collard, A., Crevoisier, C., Dufour, G., Edwards,  
548 D., Faijan, F., Fourrié, N., Gambacorta, A., Goldberg, M., Guidard, V., Hurtmans, D.,  
549 Illingworth, S., Jacquinet-Husson, N., Kerzenmacher, T., Klaes, D., Lavanant, L.,  
550 Masiello, G., Matricardi, M., McNally, A., Newman, S., Pavelin, E., Payan, S., Péquignot,  
551 E., Peyridieu, S., Phulpin, T., Remedios, J., Schlüssel, P., Serio, C., Strow, L.,  
552 Stubenrauch, C., Taylor, J., Tobin, D., Wolf, W., and Zhou, D.: Hyperspectral Earth  
553 Observation from IASI: Five Years of Accomplishments, *Bull. Am. Meteorol. Soc.*, 93,  
554 347-370, DOI: 10.1175/BAMS-D-11-00027.1, 2012.

555 IPCC: Climate Change 2013: The physical science basis. Contribution of working group I to  
556 the fifth assessment report of the Intergovernmental Panel on Climate Change [Stocker,  
557 T.F., D. Qin, G.-K. Plattner, M. Tignor, S.K. Allen, J. Boschung, A. Nauels, Y. Xia, V.

558 Bex and P.M. Midgley (eds.)]. Cambridge University Press, Cambridge, United Kingdom  
559 and New York, NY, USA, 1535 pp., 2013.

560 Kim, S-W., Yoon, S-C., Jefferson, A., Won, J-G., Dutton, E.G., Ogren, J.A., and Anderson,  
561 T.L.: Observation of enhanced water vapor in Asian dust layer and its effect on  
562 atmospheric radiative heating rates, *Geophys. Res. Letters*, *31*, L18113,  
563 doi:10.1029/2004GL020024, 2004.

564 Kim, S.-W., Chazette, P., Dulac, F., Sanak, J., Johnson, B., and Yoon, S.-C.: Transport and  
565 vertical structure of aerosols and water vapor over West Africa during the African  
566 monsoon dry season, *Atmos. Chem. Phys.*, *9*, 8017-8038, 2009.

567 Klaes, K.D., Cohen, M., Buhler, Y., Schussel, P., Munro, R., von Engel, A., Clérigh, E.,  
568 Bonekamp, H, Ackermann, J., and Schmetz, J.: An introduction to the EUMETSAT polar  
569 system, *Bull. Am. Meteorol. Soc.*, *88*, 1085–96, doi:10.1175/BAMS-88-7-1085, 2007.

570 Larson, T.V., and Taylor, G.S.: On the evaporation of NH<sub>4</sub>NO<sub>3</sub> aerosol, *Atmos. Environ.*, *17*,  
571 2489-2595, 1983.

572 Masiello, G., Serio, C., Deleporte, T., Herbin, H., Di Girolamo, P., Champollion, C.,  
573 Behrendt, A., Bosser, P., Bock, O., Wulfmeyer, V., Pommier, M., and Flamant, C.:  
574 Comparison of IASI water vapour products over complex terrain with COPS campaign  
575 data, *Meteorologische Zeitschrift*, *22*, 4, 471-487, doi:10.1127/0941-2948/2013/0430,  
576 2013.

577 Matricardi, M., and McNally, A. P.: The direct assimilation of principal components of IASI  
578 spectra in the ECMWF 4D-Var, *Q. J. Roy. Meteor. Soc.*, *140*, 573-582,  
579 doi:10.1002/qj.2156, 2013.

580 Mattis, I., Ansmann A., Müller D., Wandinger U., and Althausen D., Dual-wavelength Raman  
581 lidar observations of the extinction-to-backscatter ratio of Saharan dust, *Geophys. Res.*  
582 *Lett.*, *29*, 9, 1306, doi:10.1029/2002GL014721, 2002.

583 Ogawa, T., Shimoda, H., Hayashi, M., Imasu, R, Ono, A, Nishinomiya, S, and Kobayashi, H:  
584 IMG, Interferometric measurement of greenhouse gases from space, *Adv. Space. Res.*, *14*,  
585 25-28, 1994.

586 Pierangélo, C., Chedin, A., and Chazette, P.: Measurements of Stratospheric Volcanic Aerosol  
587 Optical Depth from NOAA/TOVS Observations, *J. Geophys. Res.*, *109*, D03207, 2004.

588 Pougatchev, N., August, T., Calbet, X., Hultberg, T., Oduleye, O., Schlüssel, P., Stiller, B.,  
589 Germain, K. St., and Bingham, G.: IASI temperature and water vapor retrievals – error  
590 assessment and validation, *Atmos. Chem. Phys.*, *9*, 6453-6458, doi:10.5194/acp-9-6453-  
591 2009, 2009.

592 Randriamiarisoa, H., Chazette, P., Couvert, P., and Sanak, J.: Relative humidity impact on  
593 aerosol parameters in a Paris suburban area, *Atmos. Chem. Phys.*, *6*, 1389–1407,  
594 doi:10.5194/acp-6-1389-2006, 2006.

595 Raut, J.-C., and Chazette, P.: Assessment of vertically-resolved PM<sub>10</sub> from mobile lidar  
596 observations, *Atmos. Chem. Phys.*, *9*, 8617-8638, doi:10.5194/acp-9-8617-2009, 2009.

597 Rood, M.J., Covert, D.S., and Larson, T.V.: Hygroscopic properties of atmospheric aerosol in  
598 Riverside, California, *Tellus*, *39B*, 383-397, 1987.

599 Royer, P., Chazette, P., Lardier, M., and Sauvage, L.: Aerosol content survey by mini-N2-  
600 Raman lidar: Application to local and long-range transport aerosols, *Atmos. Environ.*,  
601 doi:10.1016/j.atmosenv.2010.11.001, 2011.

602 Schneider, M., and Hase, F.: Optimal estimation of tropospheric H<sub>2</sub>O and  $\delta$ D with  
603 IASI/METOP, *Atmos. Chem. Phys.*, *11*, 11207-11220, doi:10.5194/acp-11-11207-2011,  
604 2011.

605 Schlüssel, P., Hultberg, T., Phillips, P., August, T. and Calbet, X.: The operational IASI Level  
606 2 processor, *Adv. Space Res.*, *36*, 982-988, 2005.

607 Shephard, M.W, Herman, R.L., Fisher, B.M., Cady-Pereira, K.E., Clough, S.A., Payne, V.H.,  
608 Whiteman, D.N., Comer, J.P., Vömel, H., Miloshevich, L.M., Forno, R., Adam, M.,  
609 Osterman, G.B., Eldering, A., Worden, J.R., Brown, L.R., Worden, H.M., Kulawik, S.S.,  
610 Rider, D.M., Goldman, A., Beer, R., Bowman, K.W., Rodgers, C.D., Luo, M., Rinsland,  
611 C.P., Lampel, M., and Gunson, M.R.: Comparison of Tropospheric Emission Spectrometer  
612 Nadir Water Vapor Retrievals with *In Situ* Measurements, *J. Geophys. Res.*, *113*, D15S24,  
613 doi:10.1029/2007JD008822, May 16, 2008.

614 Susskind, J., Rosenfield, J., Reuter, D., and Chahine, M.T.: Remote sensing of weather and  
615 climate parameters from HIRS2/MSU on TIROS-N. *J. Geophys. Res.*, *89*, 4677-4697,  
616 1984.

617 Wang, Y., Sartelet, K. N., Bocquet, M., and Chazette, P.: Modelling and assimilation of lidar  
618 signals over Greater Paris during the MEGAPOLI summer campaign, *Atmos. Chem. Phys.*  
619 *Discuss.*, *13*, 27115-27161, doi:10.5194/acpd-13-27115-2013, 2013.

620 Worden, J., Kulawik, S., Frankenberg, C., Payne, V., Bowman, K., Cady-Peirara, K.,  
621 Wecht, K., Lee, J.-E., and Noone, D.: Profiles of CH<sub>4</sub>, HDO, H<sub>2</sub>O, and N<sub>2</sub>O with improved  
622 lower tropospheric vertical resolution from Aura TES radiances, *Atmos. Meas. Tech.*, *5*,  
623 397-411, doi:10.5194/amt-5-397-2012, 2012.

624 Xu, D., Liu Z., Zhiquan, Huang, X.-Y., Min, J., and Wang, H.: Impact of assimilating IASI  
625 radiance observations on forecasts of two tropical cyclones, *Meteorology and Atmospheric*  
626 *Physics*, *122*, 1-18, doi: 10.1007/s00703-013-0276-2, 2013.



627 Zhou, D. K., Smith, W. L., Larar, A. M., Liu, X., Taylor, J. P., Schlüssel, P., Strow, L. L., and  
628 Mango, S. A.: All weather IASI single field-of-view retrievals: case study – validation with  
629 JAIVEx data, *Atmos. Chem. Phys.*, 9, 2241-2255, doi:10.5194/acp-9-2241-2009, 2009.

630

631

632 Table 1: Main technical characteristics of the WALI instrument.

Laser	Nd:Yag
Energy	60 mJ at 355 nm
Frequency	20 Hz
Reception channels	Elastic total 354.67 nm Elastic $\perp$ 354.67 nm Raman-N <sub>2</sub> 386.63 nm Raman-H <sub>2</sub> O 407.5 nm
Reception diameters	15 cm
Field of view	~2.3 mrad
Full overlap	~300 m
Detector	Photomultiplier tubes
Filter bandwidths	0.2 - 0.3 nm
Vertical sampling	0.75 m (analog) 15 m (photon counting)
Vertical resolution used for this study	~ 40 m
Acquisition system	PXI technology at 200 MHz

633

634 Table 2: List of the coincidence numbers (CN) and description of the associated aerosol layer  
635 synoptic origin during the HyMeX experiment (2012 fall period).  $D$  represents the distance  
636 between the ground-based lidar and the center of the 12 selected IASI pixels.  $N$  is the number  
637 of available averaged IASI profiles. The wettest (driest) coincidences are in bold (italic). The  
638 presences of dry layer (DL) and residual particle layer (RPL) are indicated.

(CN) Month/Day - LT	$D$ (km)	$N$	Observation
<b>(1)</b> <b>09/19 - 23:03</b>	0.6	8	Atlantic-Spain origin, RPL below 2 km DL between 3 and 4 km, air mass off Eastern African coast
<b>(2)</b> <b>09/20 - 22:42</b>	2.4	12	Atlantic - Spain origin DL between 2 and 4 km, air mass along Eastern African coast Subsidence between ~0 and 3 km above Southern Spain
(3) 09/22 - 21:59	19.3	12	Saharan origin between 1 and 5 km (Algeria-Morocco) DL between 1 and 4 km, air mass along Eastern African coast Strong ascent from ~0 to 3 km above Morocco
(4) 09/24 - 22:59	2.8	6	Atlantic - Spain origin with a RPL below 1.5 km (from Valencia) Strong subsidence from ~4 to 0 km
(5) 09/25 - 22:39	3.9	12	Atlantic-Southern Spain origin Below 1 km, RPL from Gibraltar with strong subsidence from ~3 km
<b>(6)</b> <b>09/30 - 22:33</b>	55.2	6	Between 2 and 5 km, Saharan, France and Spain origin Below 1 km, RPL from Gibraltar (petrochemistry) Strong subsidence from 8 to 4 km above Moroccan sea coast
(7) 10/01 - 22:15	8.3	11	Northern Spain - Southwestern France origin RPL below 3 km from Valencia-Barcelona
(8) 10/03 - 23:12	5.2	12	Spain origin RPL below 2 km from Valencia coast
(9) 10/04 - 22:51	2.6	12	Saharan (Morocco) and Southern - Spain origin DL between 2 and 4 km
<b>(10)</b> <b>10/08 - 23:09</b>	2.1	9	Tropical Atlantic - Spain origin DL below 4 km, mainly between 2 and 4 km May be Saharan air masses off African west coast
(11) 10/09 - 22:48	6.5	12	Tropical Atlantic - Spain origin Below 2 km, RPL from Valencia-Barcelona coast
(12) 10/13 - 23:06	8.5	11	Atlantic - Northern Spain origin RPL from Barcelona coast
(13) 10/16 - 22:03	45.8	6	Atlantic-Spain origin Strong subsidence from 4 to 1 km over Spain RPL from Valencia-Barcelona coast
(14) 10/17 - 23:24	5.2	11	Saharan origin with a strong DL below 3 km Strong subsidence from 4 to 0 km over Sahara
(15) 10/23 - 22:57	3.3	9	Spain origin - Long passage over the Mediterranean sea No significant aerosol layer

639

640 Table 3: Same as Table 2 for the ChArMEx experiment (2013 summer period).

(CN) Month/Day - LT	<i>D</i> (km)	<i>N</i>	Observation
(1) 06/10 - 21:59	5.8	12	Spain - Southern France origin Strong subsidence from ~6 to 2 km
(2) <b>06/11 - 23:18</b>	7.2	12	Atlantic - Spain origin RPL from Barcelona coast
(3) 06/12 - 22:57	3.5	12	Atlantic - Spain origin Strong subsidence from ~8 to 5 km
(4) 06/13 - 22:36	5.0	12	Atlantic-Southern France origin RPL from Perpignan coast Dry air mass at ~3 km (drying over the Pyrenees)
(5) <b>06/14 - 22:15</b>	2.2	12	France origin below 1 km Tropical Atlantic - Southern Spain origin above 1 km RPL from Valencia coast
(6) <b>06/15 - 21:54</b>	4.4	12	Mediterranean origin below 1 km Atlantic (off Moroccan coast) - Southern Spain origin above 1 km DL between ~2.5 and 4 km
(7) <b>06/16 - 23:15</b>	11.2	12	Mediterranean origin below 1 km Morocco-Algeria origin above 1 km DL between 1 and 5 km
(8) <b>06/17 - 22:54</b>	4.0	10	Atlantic - Morocco origin with a small DL ~0-7 km. Likely dust uptake between 0 and 4 km
(9) 06/20 - 23:33	47.1	12	Spain origin RPL from Valencia coast
(10) 06/22 - 22:51	3.0	12	Atlantic - Spain - Southwestern France origin Strong subsidence between ~9 and 4 km RPL from Barcelona coast
(11) 06/24 - 22:09	8.2	12	Atlantic - Spain - Southwestern France origin Strong subsidence between ~7 and 0 km Dry air mass at ~2.5 km RPL from Barcelona coast
(12) 06/25 - 23:27	29.0	12	Atlantic - Spain - Southwestern France origin Strong subsidence between ~8 and 4 km RPL from Perpignan coast
(13) 06/27 - 22:48	14.3	6	Northern Atlantic - France origin RPL from Perpignan coast
(14) 06/30 - 23:24	19.4	12	Northwestern Atlantic - France origin
(15) 07/02 - 22:42	4.2	10	France - Spain - Morocco origin with a DL between 3 and 5 km Strong wind-shear - RPL from Montpellier and Barcelona coasts

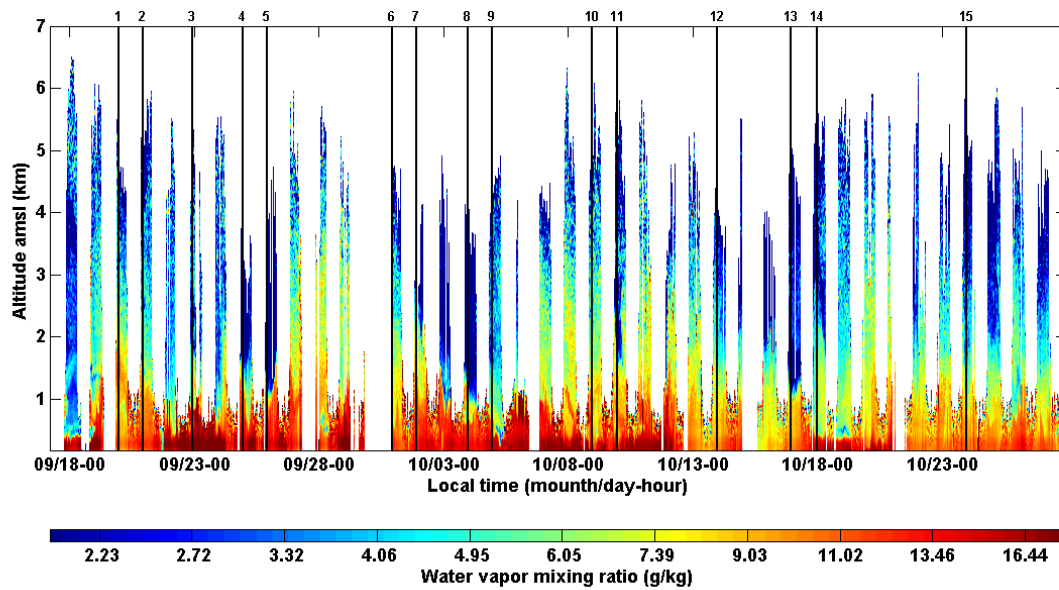
641

642 Table 4: Scores on the WVMR retrieval for the inter-comparisons between WALI and IASI  
 643 (WALI-IASI), and WALI and ECMWF (WALI-ECMWF). The results are given for different  
 644 atmospheric layers in terms of COR and RMSE for the two time periods.

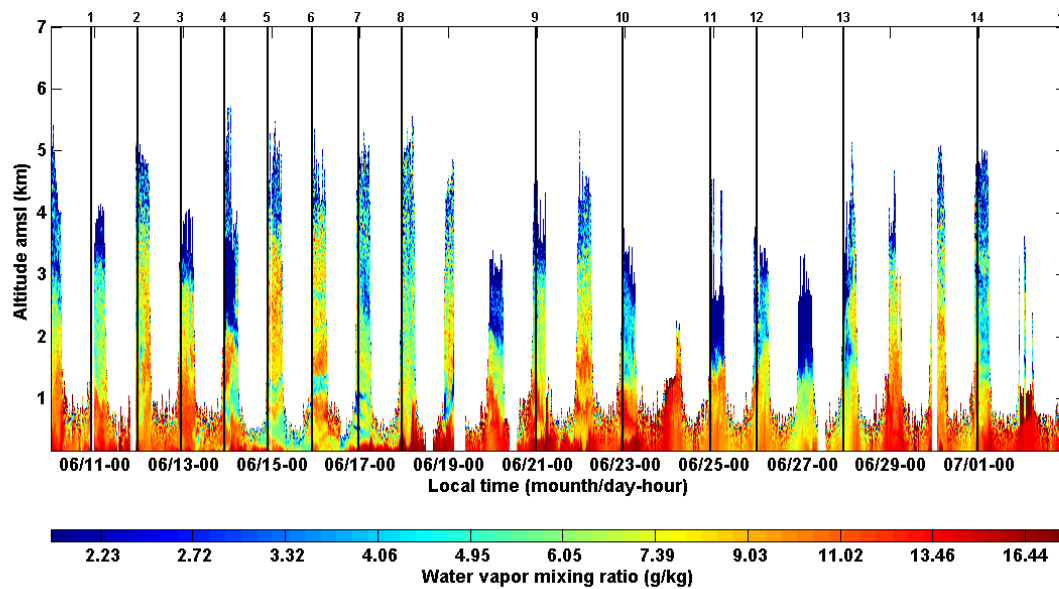
Altitude range (km)	COR		RMSE (g/kg)	
	WALI-IASI	WALI-ECMWF	WALI_IASI	WALI-ECMWF
September-October 2012				
0.5-2.0	0.37	0.73	1.42	1.15
2.0-5.0	0.77	0.81	0.66	0.55
5.0-7.0	0.78	0.73	0.25	0.26
0.5-7.0	0.70	0.77	0.78	0.65
June-July 2013				
0.5-2.0	0.15	0.74	1.80	2.42
2.0-5.0	0.70	0.91	1.34	1.16
5.0-7.0	0.75	0.77	0.67	0.66
0.5-7.0	0.59	0.82	1.28	1.43

645

646



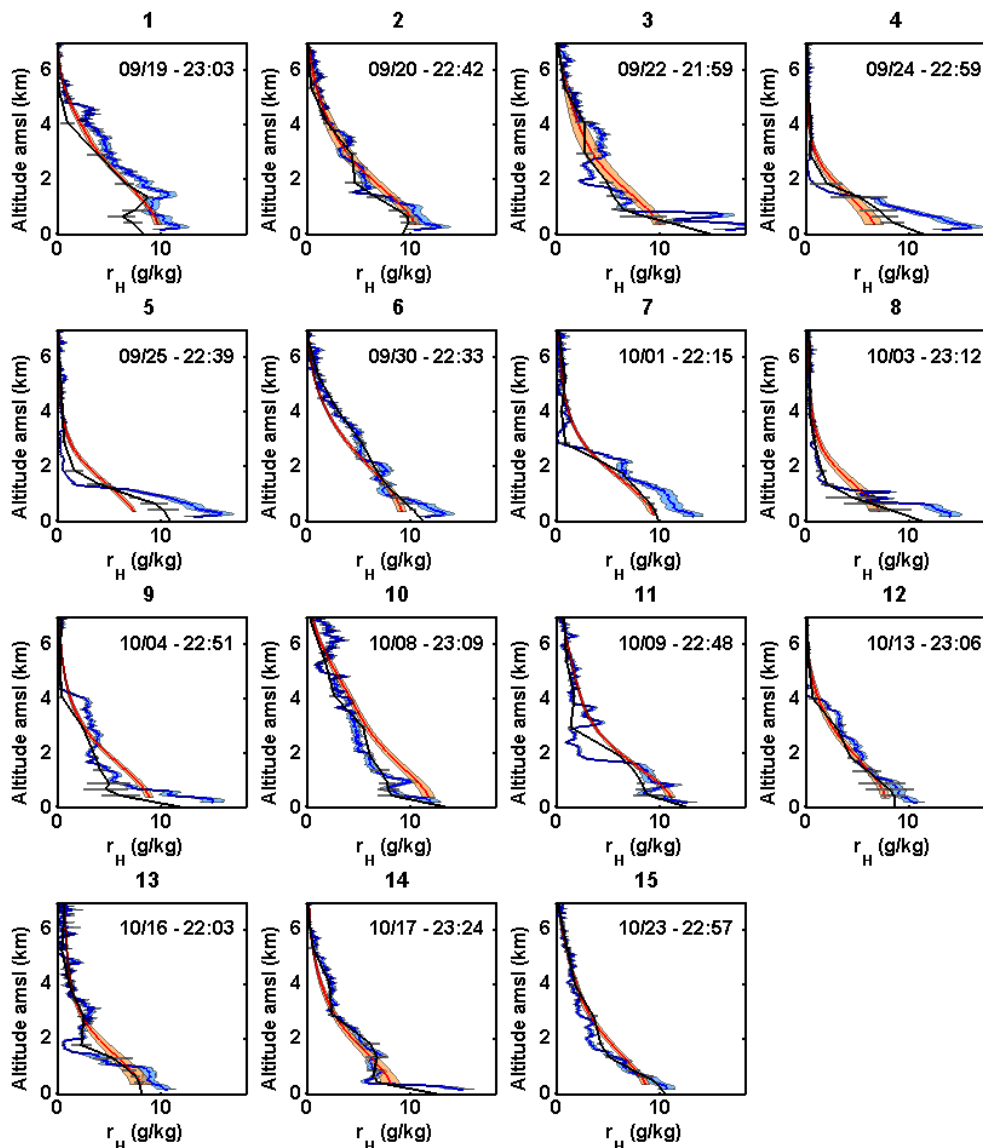
647



648

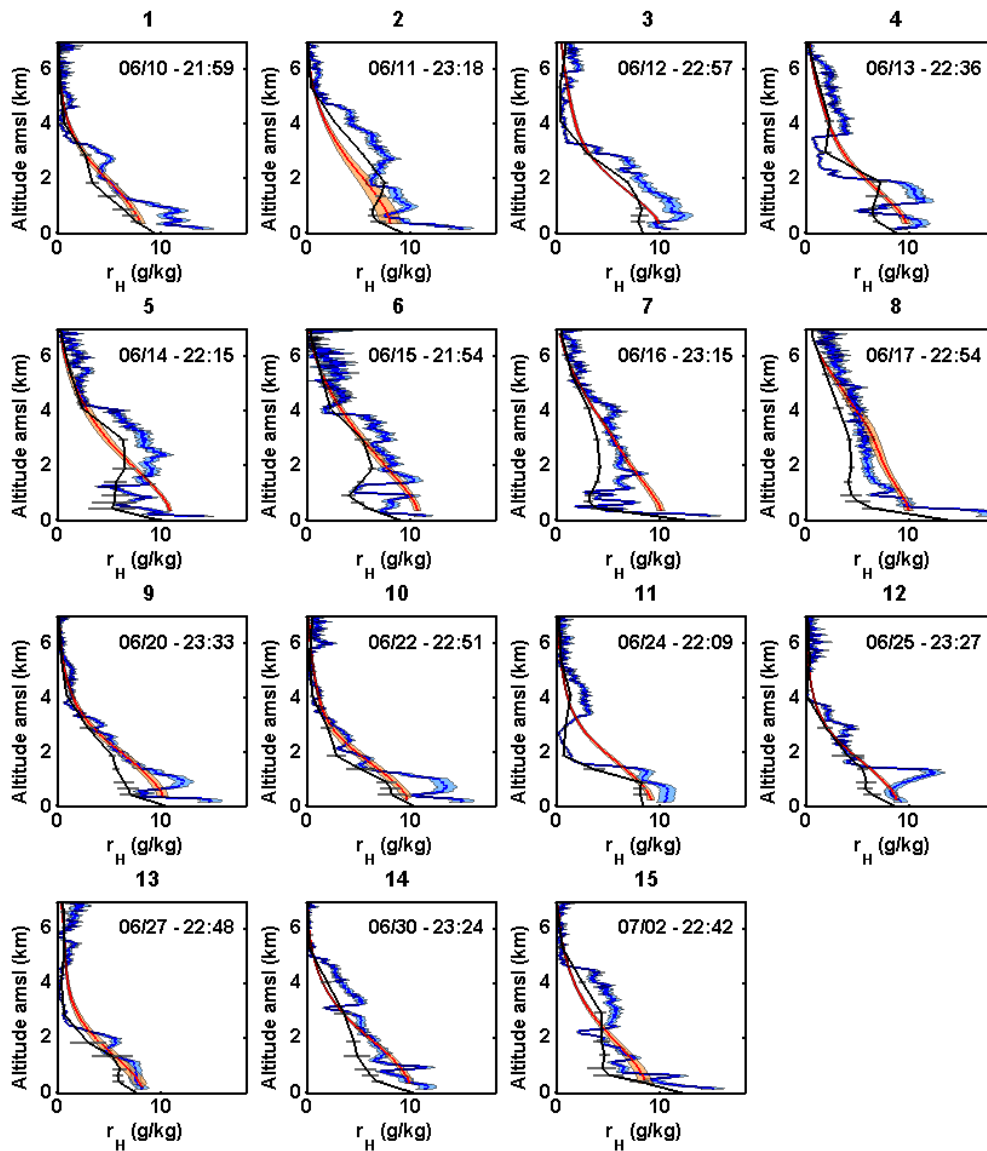
649 Figure 1: Time localization of the IASI profiles used for the inter-comparisons (vertical black  
 650 lines identified with the CN at the top) with respect to the temporal WALI lidar WVMR (in  
 651 g/kg) retrieval evolution as a function of altitude (in km) during the HyMeX (up) and  
 652 ChArMEx (down) periods. Lidar profiles are given with a high temporal resolution of 5  
 653 minutes averaging. The color bar ranges from low water vapor mixing-ratio (blue) to high  
 654 ones (red).

655

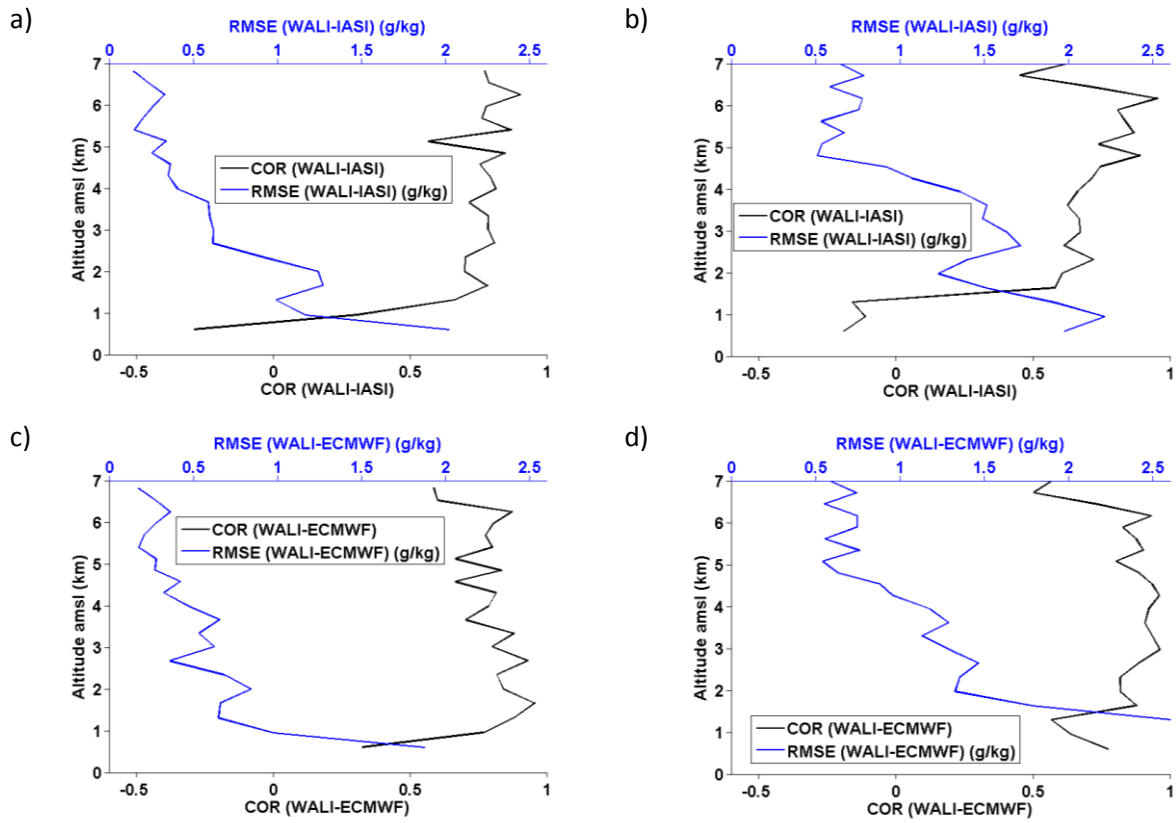


657

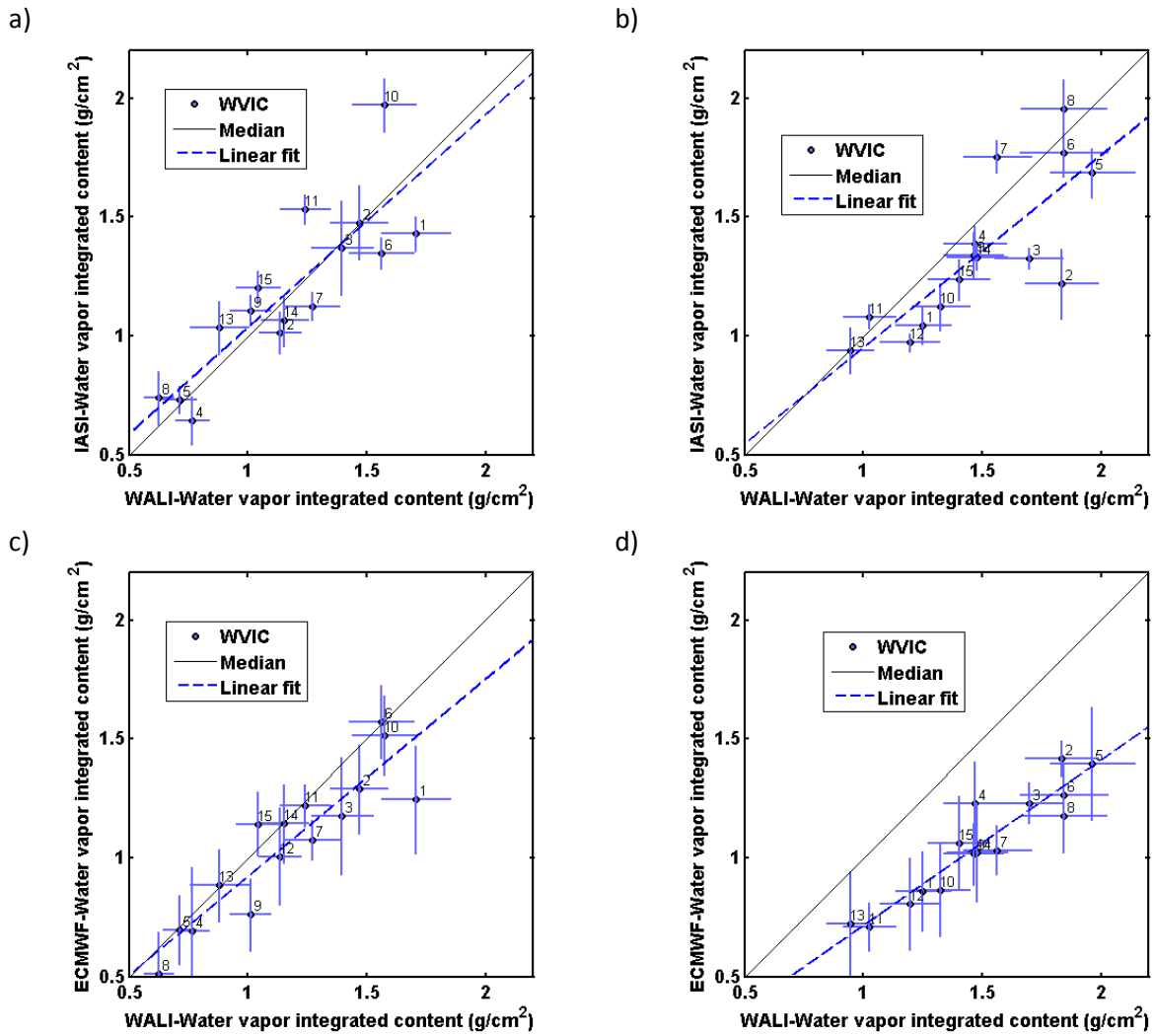
658 Figure 2: Comparisons of WVMR vertical profile retrieval as a function of altitude between:  
 659 IASI (red), WALI lidar (blue) and ECMWF analysis (black), over Menorca during the  
 660 HyMeX experiment (September and October 2012). The date and time of the IASI and WALI  
 661 measurements are also given for each panel of individual profile in the form month/day  
 662 HH:MM. The CN is given at the top of each figure.







666 | Figure 4: Evolution as a function of altitude of the RMSE in g/kg (blue) and COR (black)  
 667 | between IASI and WALI WVMR retrievals for HyMeX (a) and ChArMEx (b) periods, and  
 668 | between WALI WVMR retrieval and ECMWF analysis for HyMeX (c) and ChArMEx (d)  
 669 | periods.



670

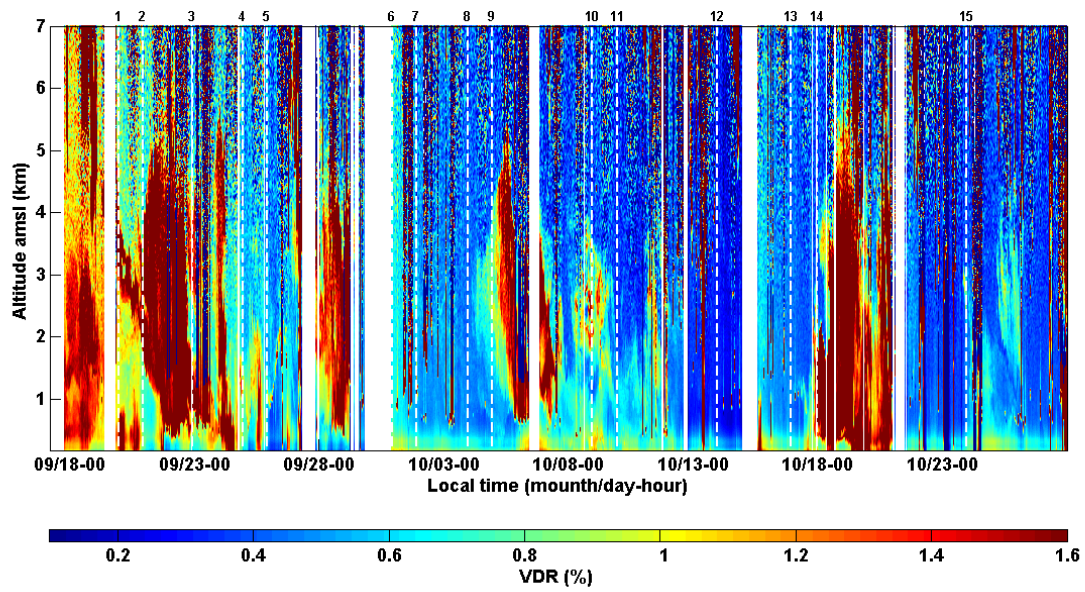
671 Figure 5: Water Vapor Integrated Content (WVIC in g/cm<sup>2</sup>) as measured by WALI lidar

672 against IASI WVIC retrieval for HyMeX (a) and ChArMEx (b) periods and against ECMWF

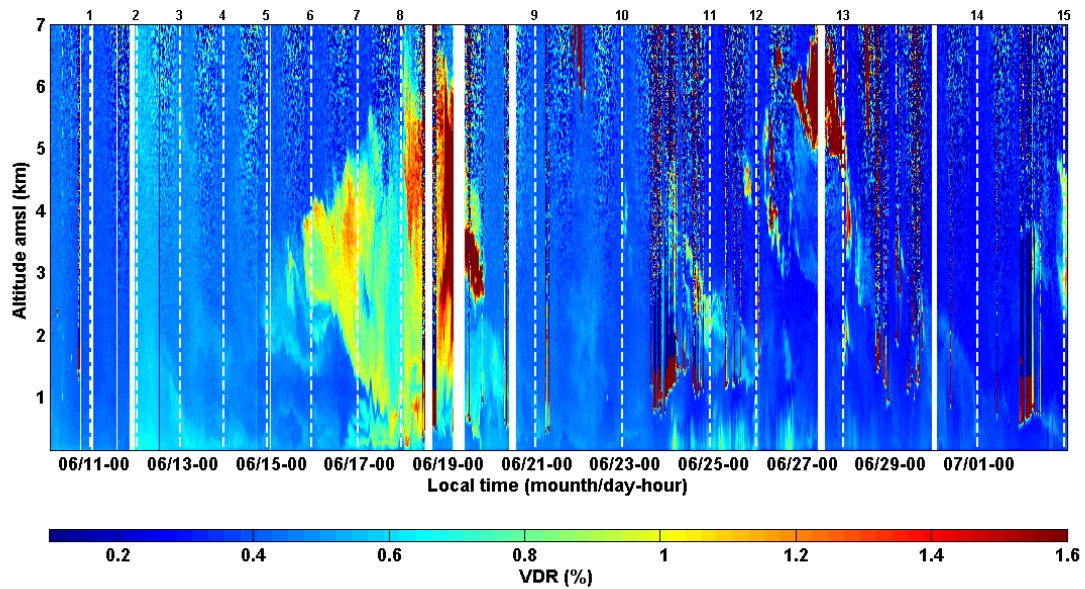
673 WVIR for HyMeX (c) and ChArMEx periods (d). Line styles are given in each individual

674 figure legend.

675



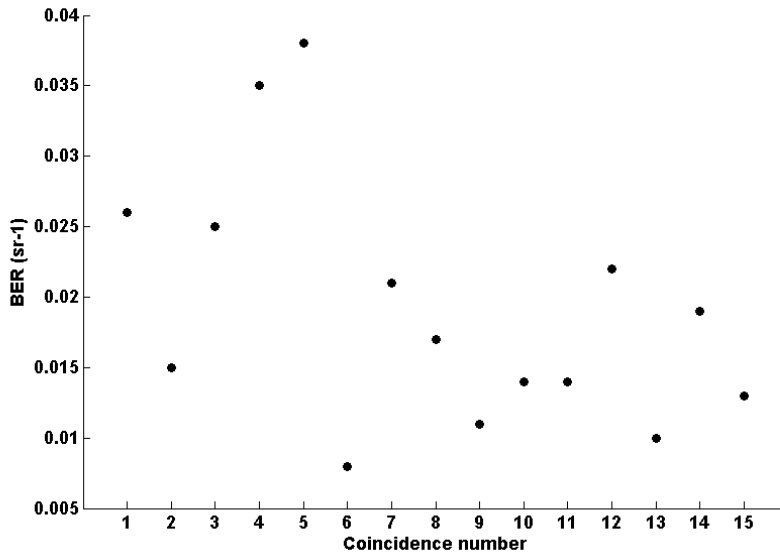
676



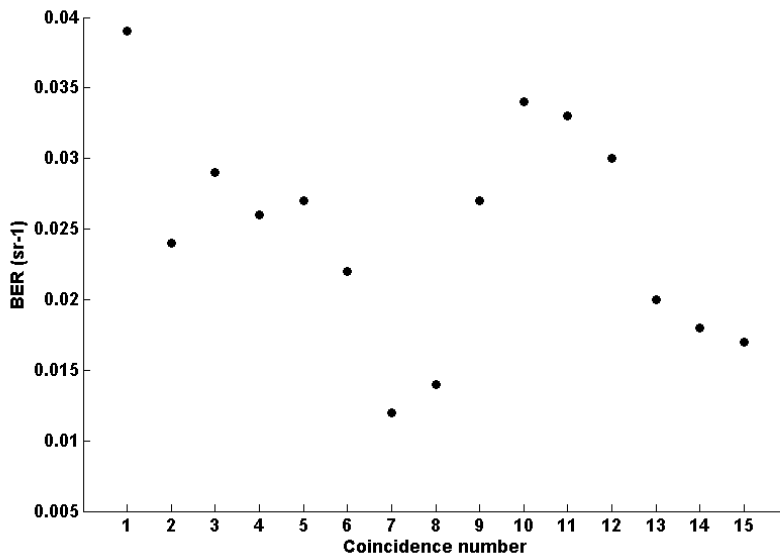
677

678 Figure 6: Volume Depolarization Ratio (VDR in %) evolution as a function of altitude (in km)  
679 during HyMeX (up) and ChArMEX (down) experiments comparisons. The vertical white  
680 dotted lines identify the coincidences with the CN at the top. The color bar ranges from low  
681 VDR (blue) to high ones (red).

682

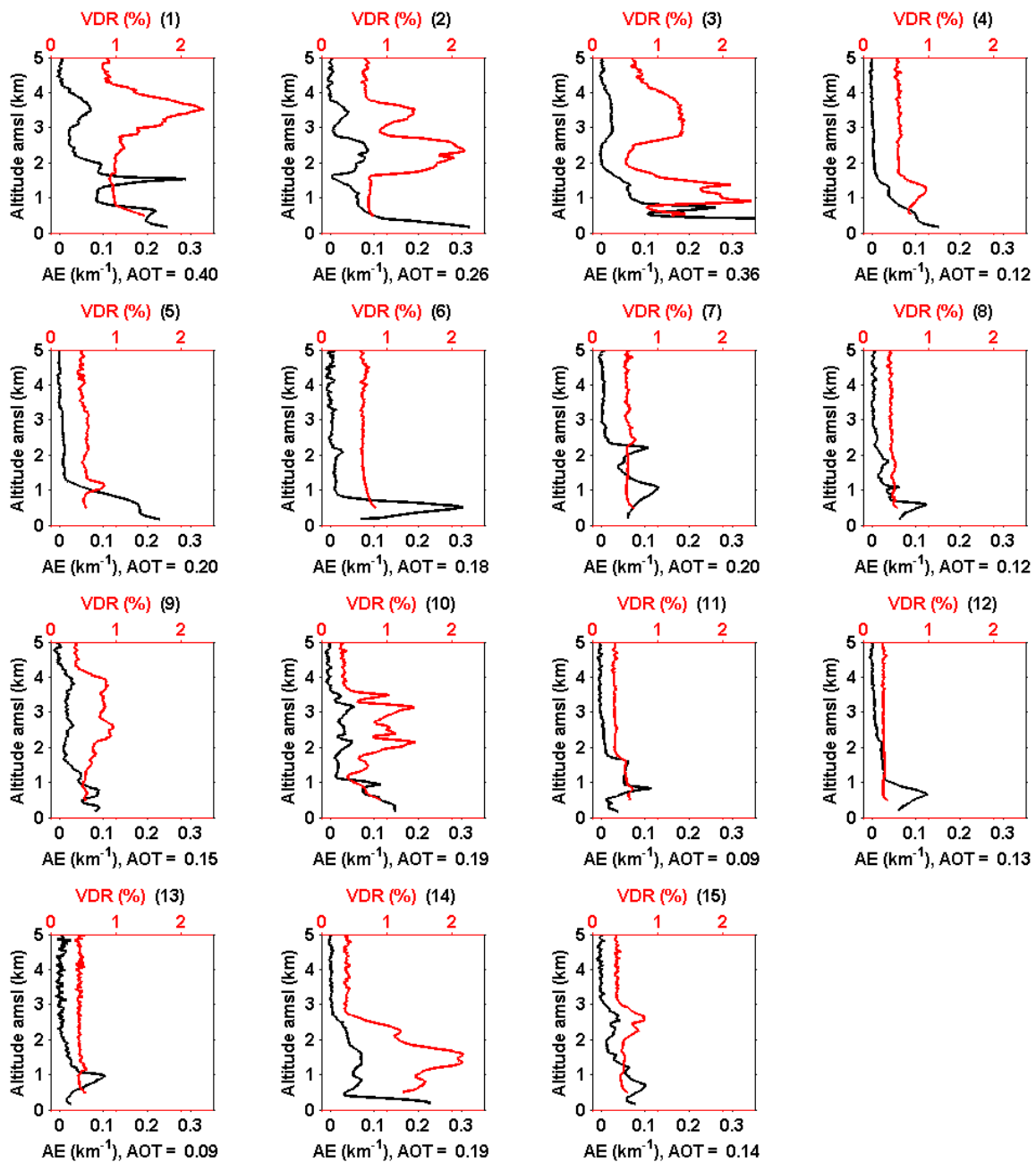


683



684

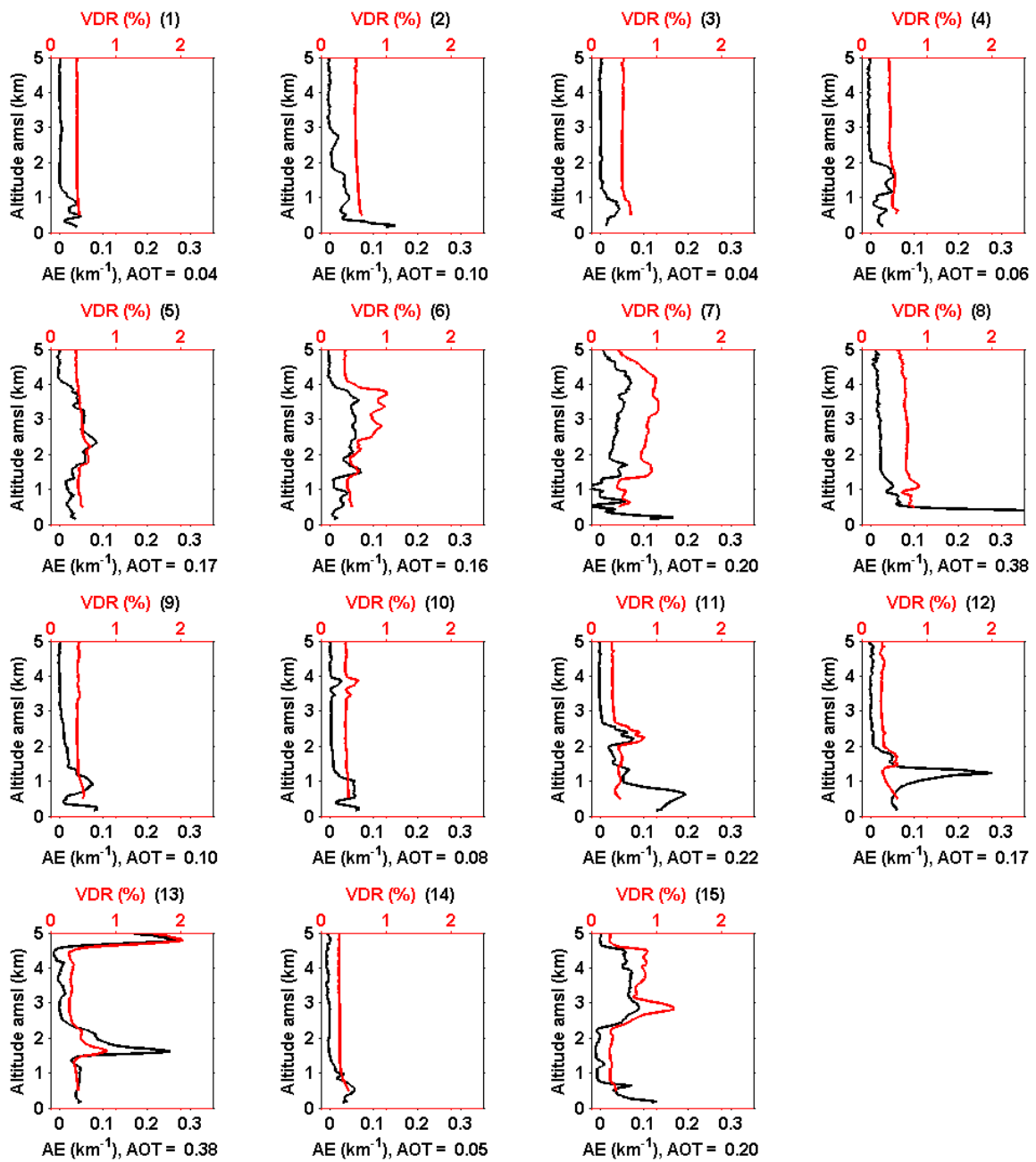
685 Figure 7: Column Backscatter to Extinction Ratio (BER in sr<sup>-1</sup>) derived from WALI temporal  
 686 evolution for the different inter-comparisons exercises during HyMeX (up) and ChArMEx  
 687 (down) experiments. Abscissa represents the CN.



688

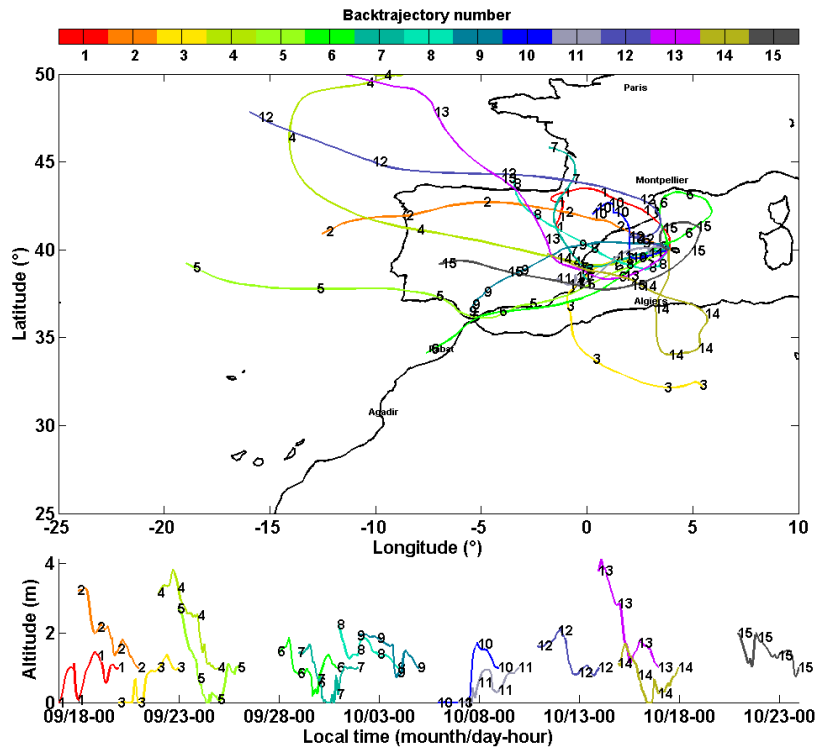
689 Figure 8: Aerosol extinction coefficient (AE in  $\text{km}^{-1}$ , black lines) and Volume Depolarization  
 690 Ratio (VDR in %, red lines) as a function of altitude for the inter-comparisons cases during  
 691 HyMeX experiment. For each individual case, the Atmospheric Optical Thickness (AOT) is  
 692 also reported. The CN is given in black at the top of each figure.

693

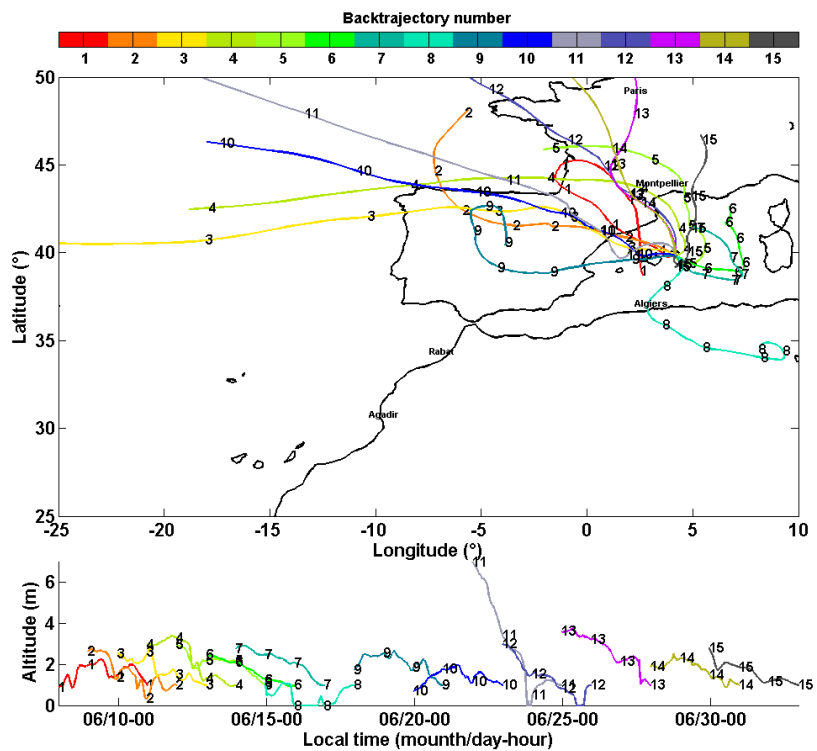


694

695 Figure 9: Same as Figure 8 for the ChArMEx experiment (June and July 2013).



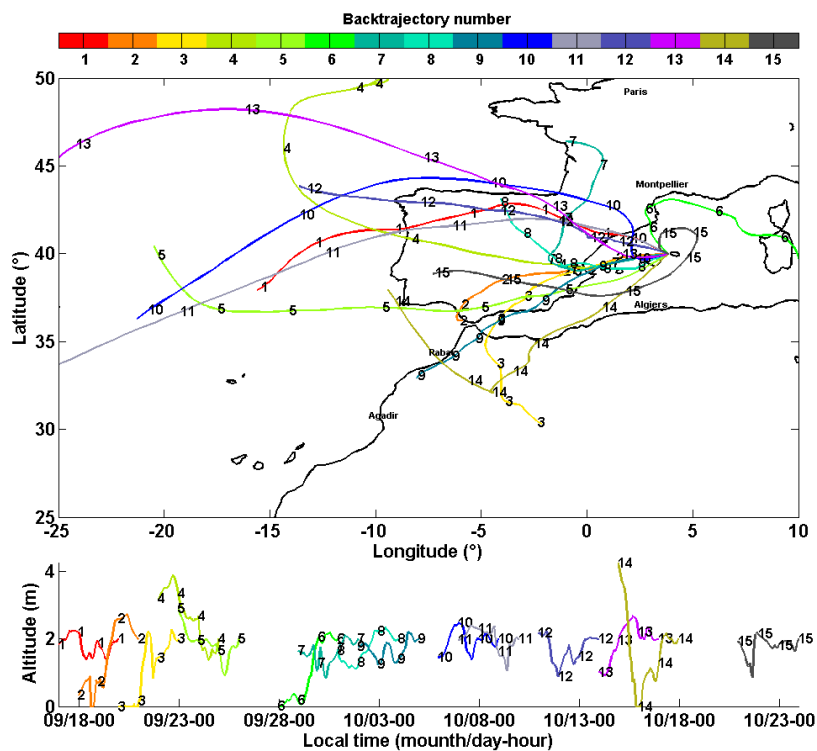
696



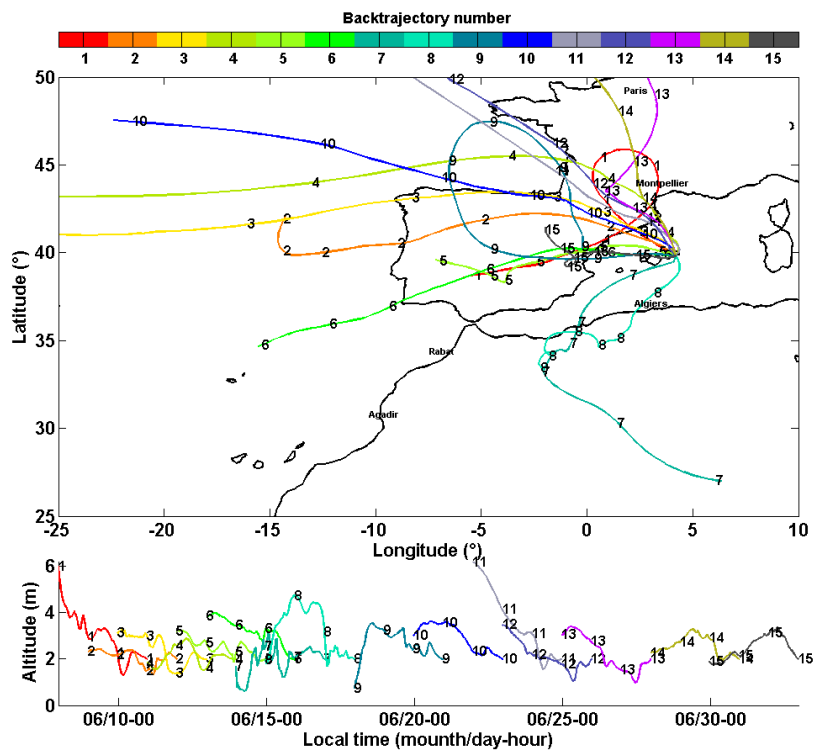
697

698 | Figure 10: Back trajectories for each CN identified by the number shown on the curves. They  
 699 | have been computed using the Hysplit model (courtesy of NOAA Air Resources Laboratory;  
 700 | <http://www.arl.noaa.gov>). The end locations of the air masses are for the sites of Ciutadella

701 (up) and Mahon (down) for the HyMeX and ChArMEx time periods, respectively, at the  
702 altitudes of 1 km amsl.



703

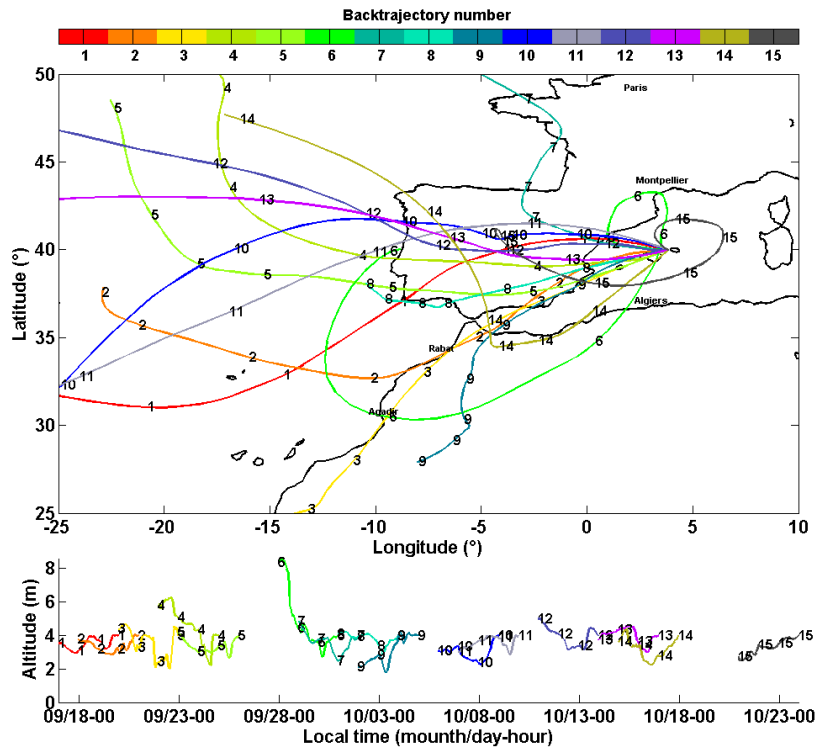


704

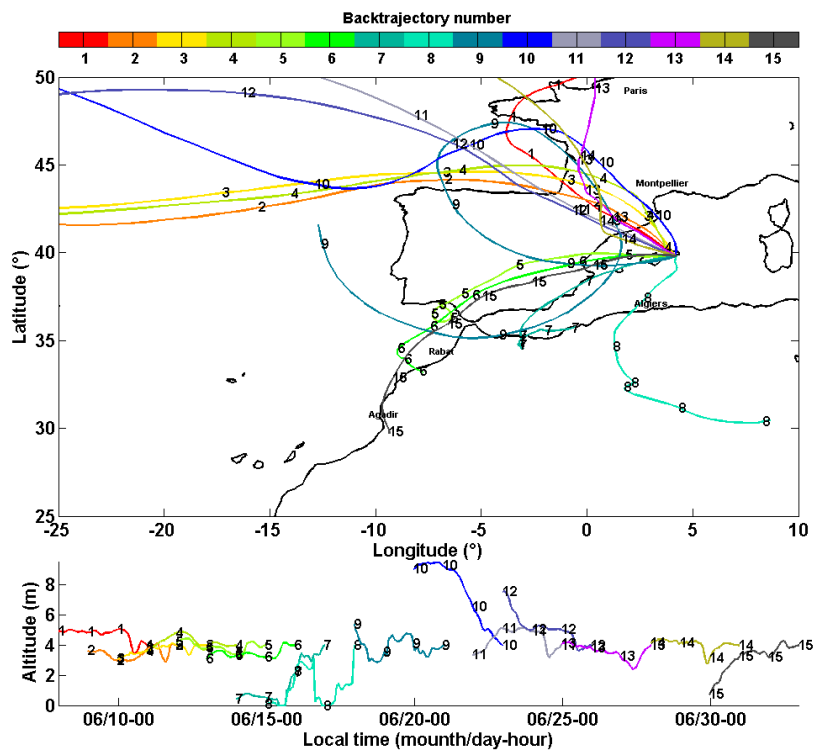
705 Figure 11: Same as Figure 10 for 2 km amsl.







707



708

709 Figure 12: Same as Figure 10 for 4 km amsl.